

UNIVERSITAT DE VALÈNCIA  
DEPARTAMENT DE FÍSICA ATÒMICA, MOLECULAR I NUCLEAR  
INSTITUT DE FÍSICA CORPUSCULAR



VNIVERSITAT  
DE VALÈNCIA

**Developing an automate procedure  
for the time calibration  
of the ANTARES Neutrino Telescope**

Trabajo de Fin de Máster dirigido por Juan Zúñiga Román

Agustín Sánchez Losa

*Curso Académico 2009/2010*



*A mi madre y a mi lala.*

*Photons can be absorbed  
or cosmic rays can be deflected,  
be neutrino my friend.*



# Agradecimientos

Es difícil resumir en pocas palabras a todas las personas que han influido en que este trabajo haya sido llevado a buen término. Quien más quien menos ha logrado ayudar a recuperar los ánimos necesarios para continuar en los momentos de flaqueza y hacerme sentirme dichoso de su compañía. Por eso a las almas anónimas, amistades que se saben de sobra aquí aludidas, quedarán en el tintero pero no en el olvido. Mi individual agradecimiento a todos ellos, os debo más de lo que puede ser agradecido.

Mi más sincero agradecimiento para aquellos que confiaron en mí al comienzo para hacer esto y que tuvieron la suficiente paciencia para no perder dicha confianza. Gracias a los compañeros del grupo, con los cuales he compartido dichas y desdichas, vosotros hacéis que me sepa afortunado de estar en el grupo de ANTARES del IFIC. Gracias a Juanjo por acogerme en el grupo y a Juande por tu predisposición a ayudarme siempre que te lo solicité.

Especial mención tienen las dos personas que más me han ayudado significativamente a terminar mi tarea. A mi director de tesis de máster, Juan, muchísimas gracias por las incontables correcciones, recomendaciones y en general toda ayuda tan diligentemente dada, sin la cual esta tesis no habría sido posible como tal, y por todo el interés, orientación y ayuda brindados desde antes del comienzo del máster y que han hecho posible que acabara donde he acabado. Y muchísimas gracias a Paco, maestro de entre los maestros de la calibración de ANTARES, del cual he aprendido casi todo lo que sé al respecto, gracias por tu paciente predisposición a todas horas y por haberme hecho tan fácil heredar dichas labores, que sepas que no importa lo lejos que te vayas, seguiré acosándote allá donde estés con mis dudas.

Y para terminar mi más sentido agradecimiento a la que siempre ha sido mi verdadera familia y que con su apoyo y comprensión han hecho posible que a pesar de las adversidades continúe persiguiendo el sueño de ser físico. Gracias mamá. Gracias lala.

Eternamente agradecido,  
Agustín



# Contents

<b>Introduction</b>	<b>1</b>
<b>1 Astrophysics, neutrinos and telescopes</b>	<b>3</b>
1.1 Neutrinos in astrophysics . . . . .	3
1.2 Expected Neutrino sources . . . . .	4
1.3 Detecting neutrinos from astrophysical sources . . . . .	5
<b>2 The ANTARES neutrino telescope</b>	<b>9</b>
2.1 The ANTARES detector . . . . .	9
2.2 Optical Modules . . . . .	10
2.3 The Storey . . . . .	11
2.4 The Line . . . . .	11
2.5 The Junction Box and the electro-optical cable . . . . .	12
<b>3 Time calibration of the ANTARES detector</b>	<b>15</b>
3.1 The ANTARES time calibration system . . . . .	15
3.2 Readout electronics: The ARS . . . . .	18
3.3 Effects to consider in the signal processing . . . . .	21
<b>4 Time calibration with the Optical Beacon System</b>	<b>25</b>
4.1 Introduction . . . . .	25
4.2 Previous calibration procedure . . . . .	25
4.3 Automation of the time calibration procedures . . . . .	27
4.4 Intraline calibration . . . . .	30
4.5 Interline calibration . . . . .	33
<b>Conclusions</b>	<b>39</b>
<b>A Figures for the intraline calibration</b>	<b>41</b>
<b>B Interline with the Laser OB</b>	<b>45</b>
<b>C Interline with the LED OB</b>	<b>49</b>
<b>Bibliography</b>	<b>51</b>



# Introduction

The understanding of astrophysical phenomena has always been based on the observation of messengers arriving to the Earth. The first sights about what happens further up above our heads came from the light that reach us from the stars and that we can see with our naked eyes. Since merely the last century, we have started to explore what is beyond our sky using different wavelengths or even different particles from the photon as the cosmic rays. Nowadays, we can “see” the universe not only in the optical, but in a well established whole variety of wavelengths and, more recently, with cosmic rays.

But these messengers have some drawbacks that make not easy to obtain the information that originally they carried out. Photons can be absorbed by the matter in their way to the Earth. Cosmic rays can be deflected by the magnetic fields or deviated by matter interaction, hiding their original source. These facts imply that the most part of the universe is still undercover to us.

Now it is when one of the most subtle particles known by the mankind comes to the scene. Neutrinos are elusive particles, still not well known at all, that hardly interact with the matter and the magnetic fields. The universe picture in neutrinos is practically transparent and not distorted. If our experiments could detect them like our eyes detect the photons, we could have a really clear view of the universe. They are produced everywhere, specially in high energy environments, like supernova, accretion discs or any other event. Unfortunately, the feature that makes them so useful to see their sources neatly everywhere in the universe, is the same that makes so difficult to detect them. We need very big detectors, with a great amount of target mass, and with the lowest background as possible, to detect them with enough statistic.

That huge and remarkable goal has been faced by detectors<sup>1</sup> since the 80’s, but their ideas and concepts go back at the 60’s, when in the annual international conference of high energy physics at Rochester, M. A. Markov proposed for the first time the use of the oceans as target material to detect neutrinos, using the Cherenkov light emitted by the muons resulting from neutrino matter interactions, and detecting such light with a matrix of photomultipliers distributed in a volume of at least  $1 \text{ km}^3$ .

The success of a neutrino telescope depends on its pointing accuracy and this is directly related to its angular resolution. To achieve the best angular resolution, a very precise position and time calibration is required. The work I present here as my Master’s Thesis has

---

<sup>1</sup>like IMB, Kamiokande/Super-Kamiokande and SNO, experiments for low energy neutrinos (from the Sun or nuclear facilities) or like Amanda/IceCube and ANTARES/KM3NeT, experiments for high energies (from farther astrophysical sources).

consisted in the development of an automate procedure to obtain the calibration constants of the ANTARES detector by means of the optical beacon system. In the first chapter I give a brief introduction to neutrino astronomy. The second chapter is devoted to the description of the ANTARES detector and the third chapter is dedicated specifically to the time calibration. In the fourth chapter, the automate procedure is described and finally, some results are shown.

# Chapter 1

## Astrophysics, neutrinos and telescopes

### 1.1 Neutrinos in astrophysics

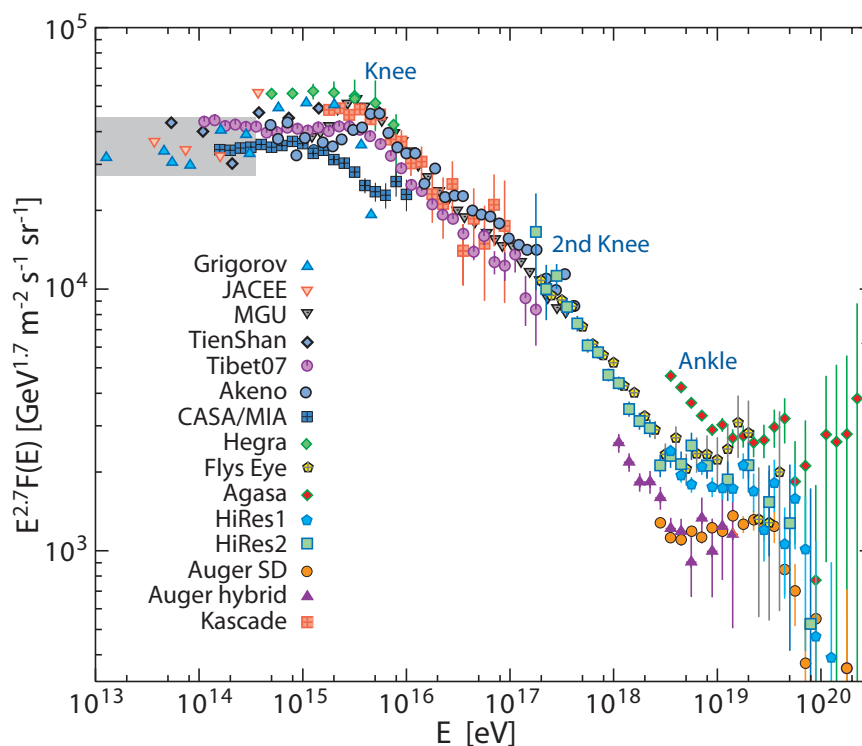
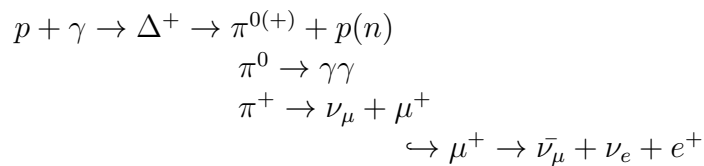


Figure 1.1: Energy spectrum of the CRs.

In 1912 Victor Hess found that the natural radiation increased with the altitude, leading to the discovery of the cosmic rays (CRs). This term was coined by Robert Millikan, who proved that their origin was extraterrestrial. Presently, we know that CRs are composed mainly by protons (89 %), helium nucleus (10 %) and heavier nucleus and electrons. The energy spectrum extends more than 10 orders of magnitude going from GeV to EeV energies (see fig. 1.1). However, the origin of CR is still uncertain. At low energies, they are deflected by the galactic magnetic field. Only at high energies it is possible to correlate their

incident direction to the Earth atmosphere with astronomical sources. Moreover, for energies above  $10^{19}$  eV protons interact with the CMB (*Cosmic Microwave Background*), effect known as GZK cutoff (*Greisen-Zatsepin-Kuzmin*), limiting their origin to basically 200 Mpc from where they are detected. On the other hand, gamma rays (GRs) are not deviated by magnetic fields but they also interact with the EBL (*Extragalactic Background Light*). For energies above 10 TeV, their range is confined to only 100 Mpc.

Neutrinos are not deviated from their sources since they are neutral particles and practically do not interact with matter, so their range is greater than the range of CRs and GRs. Neutrino production on astrophysical sources is linked to CRs by means of the so-called hadronic models. In these models, accelerated CRs, mainly protons, interact in the surroundings with the environmental photons predominantly via the  $\Delta$  resonance producing neutrinos and photons:



so CRs, GRs and neutrinos are correlated and can be used together in a multi-messenger approach, allowing flux limits predictions between them and confirming or excluding theoretical models for the production mechanisms.

Neutrino astronomy started with experiments like Homestake, which detected the first neutrinos from the Sun, and IMB and Kamiokande [1], which detected neutrinos from a supernova (SN 1987A [2]) for the first time. Currently, their successors conform the low energy neutrino astronomy, while bigger experiments as Baikal, AMANDA-IceCube or ANTARES explore the possibility to detect high energy neutrinos.

## 1.2 Expected Neutrino sources

According to their origin the most promising candidate neutrino sources can be divided into galactic and extragalactic:

### Extragalactic sources

#### AGNs

Stands for Active Galactic Nuclei. They are galaxies with a very powerful emission from their center, most probably due to the accretion matter that is falling over a supermassive black hole, converting gravitational energy into high energetic CRs, GRs and neutrino emissions. AGNs are supposed to be steady sources emitting gamma-ray, and therefore, high-energy neutrino emission is also possible. The early theoretical predictions for neutrino emission from AGNs (e.g. [3]) postulated intensities above the Waxman-Bahcall (WB) limit. However, later results were not so optimistic (e.g. [4]) giving predicted fluxes close to the WB bound. The results published by the AUGER collaboration suggest a correlation between cosmic rays and nearby cosmic sources [5]. This measurement hits the AGNs as high energy cosmic rays sources. Moreover, in

the same AUGER data, an excess of events were pointing to Centaurus A within less than  $3.1^\circ$ . This was the closest AGN included in the source list studied. Theoretical attempts in modelling the sources to infer the flux of neutrinos emitted have immediately arisen. In [6] the author claims that a neutrino detector having  $1 \text{ km}^2$  of muon effective area could detect between 0.8 and 0.02 events per year from a source with a index spectral between 2.0 and 3.0, respectively.

### GRBs

Stands for Gamma Ray Bursts. They are short and very intense flashes of GRs, lasting from milliseconds to tens of seconds, which convert them into the most energetic objects of the universe. There are two kinds of GRBs depending on their duration, short GRB (less than 2s, one each three days) and long GRB (more than 2s, one per day). While the short GRB are considered as a consequence of the merge of two compact objects, the long GRB are thought to be correlated with the born of a black hole in a supernova where a *fireball* feed by the radiation pressure expands relativistically. Protons pushed by the internal fireball shocks interact with photons, providing via the  $\Delta$  resonance pions which decay into a flux of neutrinos with energies up to  $10^{14}$  eV.

## Galactic sources

### SNRs

Stands for Supernovae Remnants. After a supernova explosion, particles are accelerated via the Fermi Mechanism [7] by the shock waves produced in the expansion of the SNR's shells. Moreover, if the final product is a neutron star, its strong magnetic field can add an additional acceleration to those particles. The last observations in GRs support the idea of the shell-type SNRs as the main source of galactic CRs.

### Galactic Center

Recently, the gamma telescope HESS [8] has confirmed the presence of a point source coincident in position with the supermassive black hole Sagittarius A\* 1001 [9, 10]. ANTARES, placed in the Mediterranean sea, can observe this part of the sky visible and make an interesting study of that region.

### Microquasars

They are binary systems formed by a compact star and a companion which provide matter to the first one, creating in this way an accretion disk and accelerating the falling matter into relativistic plasma jets in a similar way as in the case of AGNs (so the name of microquasars). Two microquasars, LS I +61 303 [11, 12] and LS 5039 [13], has been observed by MAGIC [14] as TeV GRs emitters where hadronic scenarios seems to be favoured over the leptonic ones.

## 1.3 Detecting neutrinos from astrophysical sources

A neutrino telescope is designed to detect the Cherenkov radiation produced by a charged particle (mainly muons) travelling faster than the light in the medium. They are designed as a 3D matrix of PMTs (*photomultiplier tubes*) in order to detect that radiation. From the arrival times and amplitudes of the detected photons, the direction and energy of the charged particles can be reconstructed.

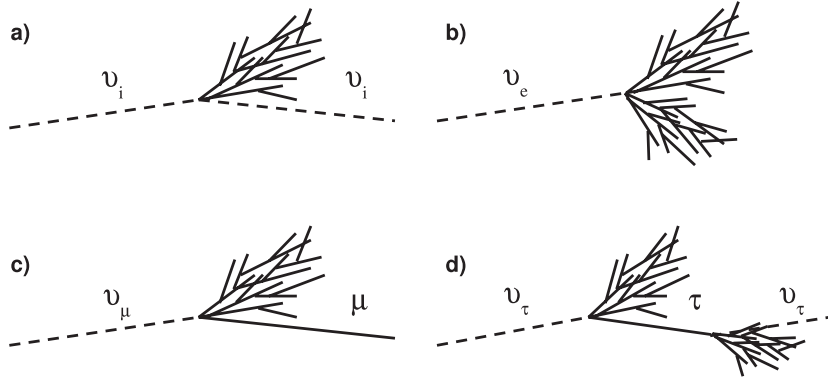
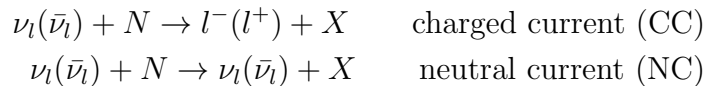


Figure 1.2: Different interactions of neutrinos with matter; (a) an example of the signal produced by a NC interaction; (b) the CC interaction of a  $\nu_e$  producing an electromagnetic cascade; (c) a  $\nu_\mu$  results in a long track of its  $\mu$  easily to detect; (d) the double bang signature of a high energy  $\nu_\tau$ .

Nuclear reactions involved in the interaction of a neutrino with matter can be:



where  $l = e, \mu, \tau$ . When a CC happens in the target medium of a neutrino telescope, the Cherenkov radiation produced by the lepton can be detected and the energy and direction of the neutrino inferred.

The energy losses of a  $\mu$  are not important below 500 GeV, which, together with its *long* lifetime, allow them to travel long distances (kilometers for TeV energies) increasing in this way the effective volume of the detector. On the other hand,  $\nu_\tau$  below a few PeV produce taus that decay very fast and can not be separated from the vertex hadronic cascade, giving a similar signal to the one produced by  $\nu_e$  which  $e$  losses its energy in an electromagnetic cascade of a few meters length. However, a more energetic  $\nu_\tau$  can create a  $\tau$  which travels long enough to separate the second cascade made by its decay, producing a clearly *double-bang* signal (see fig. 1.2).

A matrix of PMTs well calibrated in time and position can detect the Cherenkov radiation produced by the muon track, estimate its energy and reconstruct its direction. This is the direction of the muon, not the neutrino's one. However, muon and neutrino directions are aligned in  $1^\circ$  for energies greater than 1 TeV, and for  $E_\nu > 10$  TeV can be parameterized as:

$$\langle \theta_{\mu\nu} \rangle = \frac{0.64^\circ}{(E_\nu/\text{TeV})^{0.56}} \quad (1.1)$$

what makes possible to do neutrino astronomy.

### 1.3.1 Cherenkov radiation

A charged particle traversing a material faster than light on that medium emits a blue light along its trajectory. The charged particle polarizes the molecules in a constructive

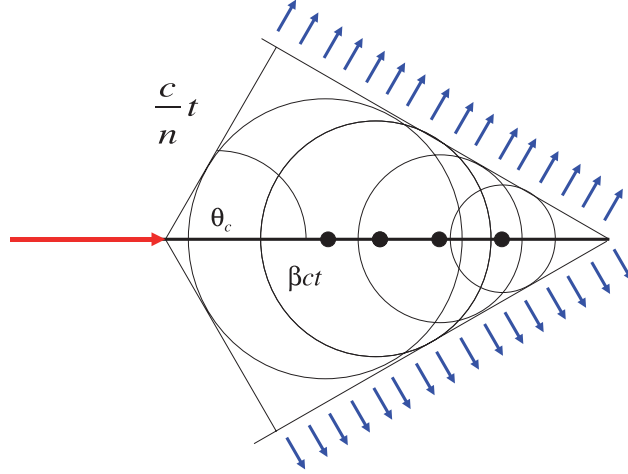


Figure 1.3: Scheme of the Cherenkov radiation.

way and an electromagnetic shock wave field is created when is travelling faster than the electromagnetic field. The condition to produce Cherenkov radiation is that the speed of the particle would be  $\beta > 1/n$ , where  $n$  is the refraction index of the environment. When constructive perturbation of the field is restored and environmental electrons return to their rest position, the light is emitted in a cone of angle (see fig. 1.3):

$$\cos \theta_c = \frac{1}{\beta n} \quad (1.2)$$

The amount of photons emitted as Cherenkov radiation by unit length and wavelength, is given by:

$$\frac{d^2 N_\gamma}{dx d\lambda} = \frac{2\pi\alpha Z^2}{\lambda^2} \left( 1 - \frac{1}{\beta^2 n^2 \lambda^2} \right) \quad (1.3)$$

for a particle of charge  $Z$  and speed  $\beta$ , in an environment of refraction index  $n$ . The number of photons is higher for shorter wavelengths, what makes Cherenkov radiation bright in the blue.

### 1.3.2 Physical background in a neutrino telescope

The main background in a neutrino telescope comes from the flux of surviving down-going muons produced by the CR interactions in the atmosphere. The atmospheric muon flux exceeds the atmospheric neutrino flux by twelve orders of magnitude. In order to reduce, as much as possible, the huge amount of atmospheric muons, neutrino telescopes are buried in water/ice at large depths (typically  $\sim 2000$  m). Even under such a thick shielding, the down-going atmospheric muon flux is still six orders of magnitude higher than atmospheric neutrinos at a depth of 2300 m water equivalent (see fig. 1.5). Therefore, only up-going events are used since only neutrinos are able to cross the entire Earth. With the aim of being more efficient to up-going tracks, the PMTs of ANTARES are  $45^\circ$  downward oriented. Consequently, ANTARES covers the opposite sight of the sky which would be seen by a conventional optical telescope located in the same latitude.

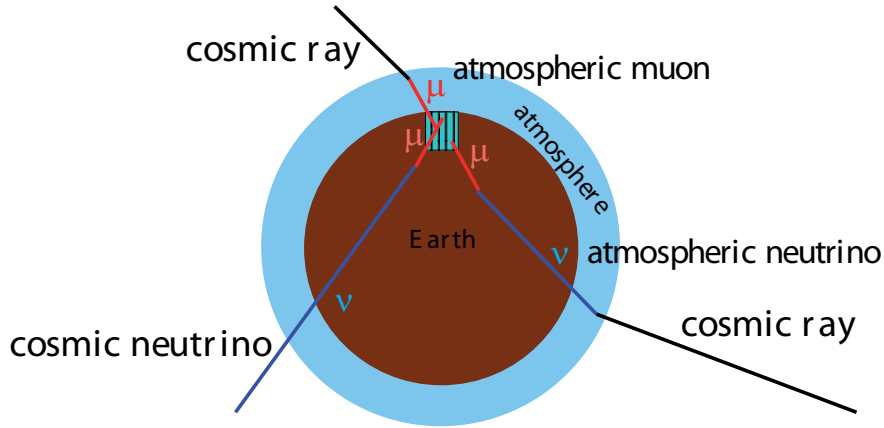


Figure 1.4: Scheme showing the detection principle. Physical background due to CR interactions with the upper shells of the atmosphere is also depicted.

The atmospheric neutrino background is more problematic since it is irreducible. However, in the sky map of neutrinos collected by the detector, atmospheric neutrinos are expected to be distributed randomly, whilst cosmic neutrinos should have privileged directions since they are expected to be produced in cosmic sources. Therefore, clusters of events will reveal the existence of cosmic neutrino sources (see fig. 1.4).

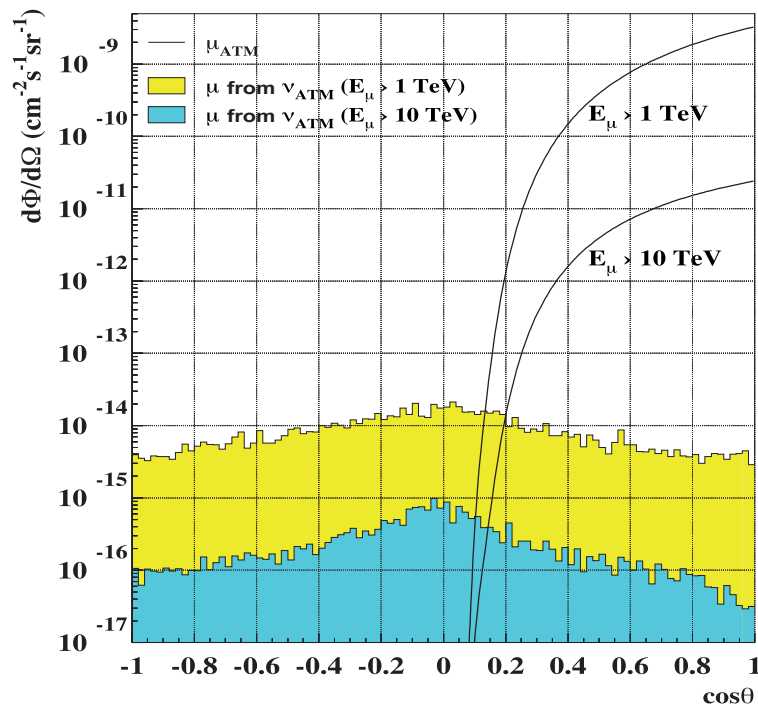


Figure 1.5: Muon and atmospheric neutrino fluxes at 2300 m water equivalent depth. Even at this depth, the muon flux dominates by six orders of magnitude the atmospheric neutrino one.

# Chapter 2

## The ANTARES neutrino telescope

### 2.1 The ANTARES detector

ANTARES (*A*stronomy with a *N*eutrino *T*elescope and *A*bys environmental *RE*Search) is an international multidisciplinary experiment sited 40 km from the coast of Toulon<sup>1</sup> (see fig. 2.1), in the south of France, and placed in the sea bed at 2500 m of depth. The ANTARES neutrino telescope is a three-dimensional matrix (see fig. 2.2) resulting in a 0.1 km<sup>3</sup> detector of high energy neutrinos with an angular resolution of 0.3° above the 10 TeV, making it the biggest neutrino telescope in the northern hemisphere and the biggest submarine one in the world [15]. The main objectives of ANTARES are the identification of astrophysics sources of neutrinos and the possibility to detect dark matter signals from the annihilation of neutralinos.

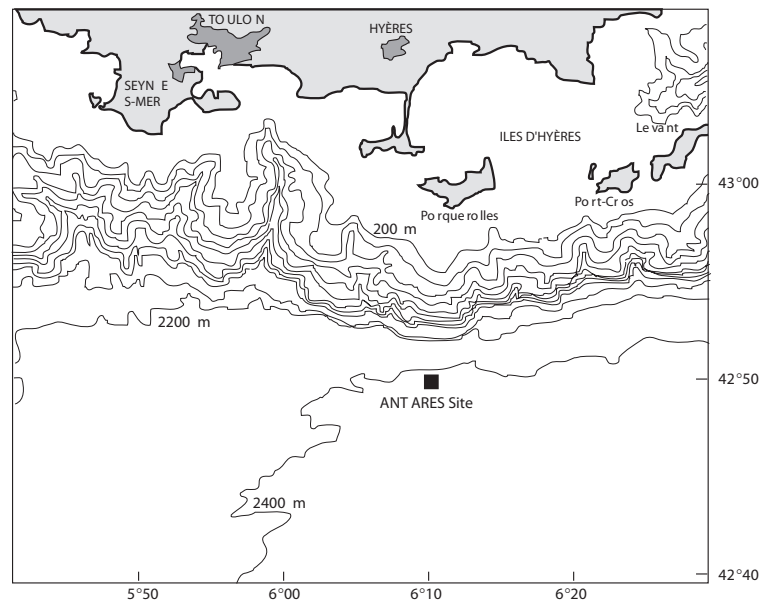


Figure 2.1: Location of the ANTARES Neutrino Telescope.

---

<sup>1</sup>At Lat 42°50'N Lon 6°10'E.

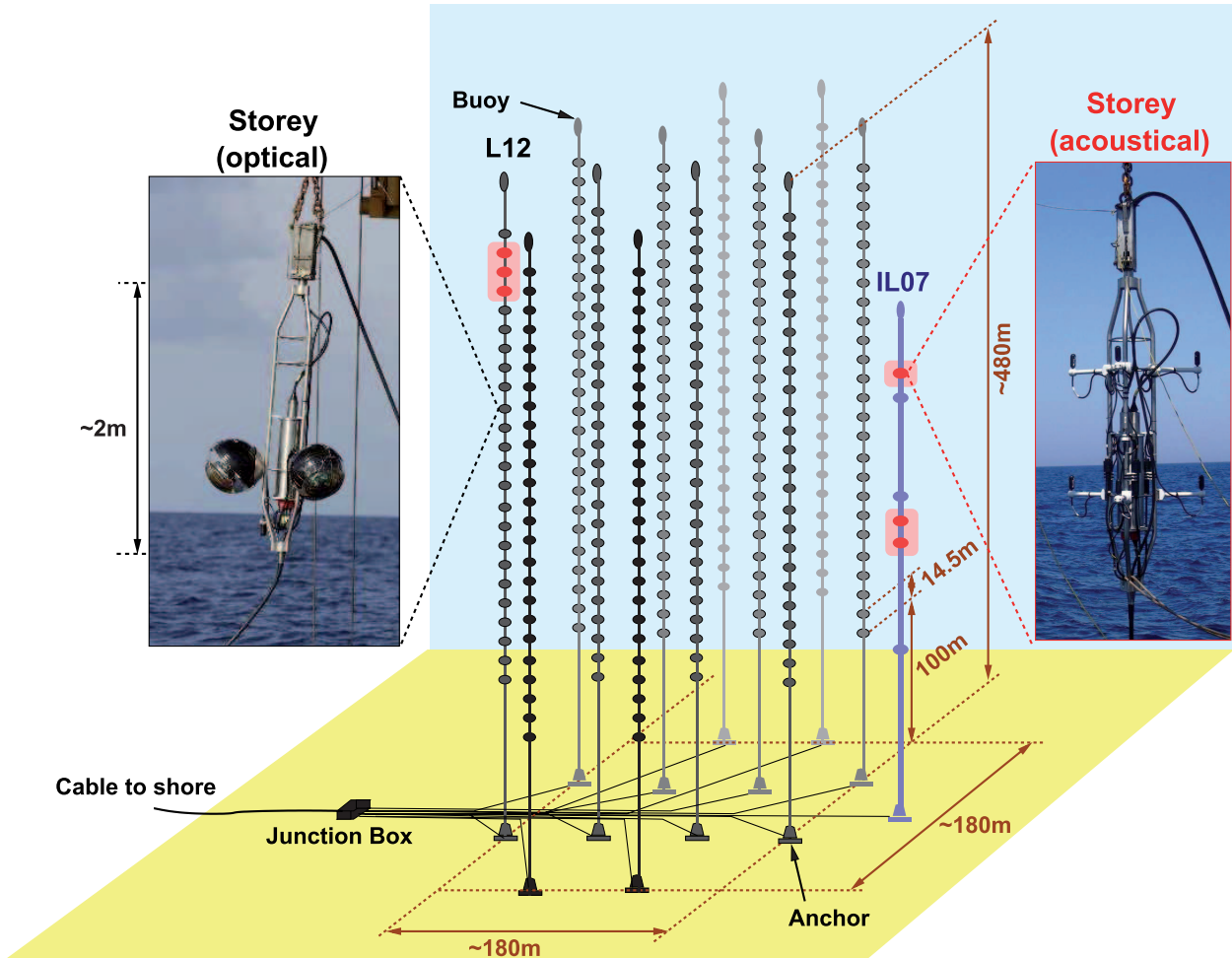


Figure 2.2: Scheme of the ANTARES Neutrino Telescope.

## 2.2 Optical Modules

The ANTARES telescope is equipped with almost 900 Optical Modules (OMs). The OM is the basic device of ANTARES [16]. It contains the PMT which detects the Cherenkov light enclosed in a glass sphere made up of borosilicate, with 41.7 cm of inner diameter and 15 mm of thickness. This sphere is devised to support high pressures of about 260 atm at normal operation and 700 atm on qualification tests. Its refractive index is 1.47 in the 300 - 600 nm range, and light transmission is  $< 95\%$  above 350 nm (see fig. 2.3).

The PMT housed in the glass sphere must meet several requirements in order to provide the best performance for physics research. Several PMT models were put under test before the final selection of the Hamamatsu R7081-20 model. This model has a 10" photocathode diameter, a gain  $< 5 \times 10^7$  working at high-voltage ( $< 2000$  V), a peak to valley ratio  $> 2$ , a transit time spread, TTS  $< 3$  ns (FWHM) and a dark noise rate  $< 10$  kHz for a 0.25 photo-electron (p.e.) threshold.

In order to reduce the influence of the Earth's magnetic field, which can degrade the TTS of the PMT, a  $\mu$ -metal cage with high magnetic permeability is also included. Fixing the  $\mu$ -metal and the PMT to the glass sphere, there is an optical gel which is highly transparent

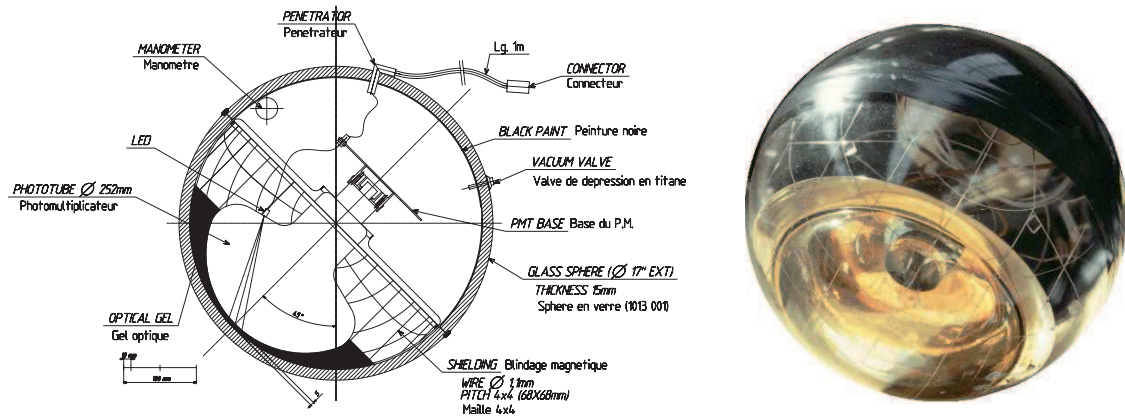


Figure 2.3: *left*: Scheme of the OMs of the ANTARES Neutrino Telescope; *right*: Picture of an OM.

and has been devised with an appropriate refraction index to reduce reflection.

## 2.3 The Storey

Each storey is composed by a triplet of OMs and a titanium container, the Local Control Module (LCM), which contains and protects the associated electronics from the water pressure. Some storeys have additional instruments: receiving Rx hydrophones (5 per line) devised for the acoustic positioning system, and an LED Optical Beacon (4 per line) for timing calibration purposes. The triplet of OMs are equally spaced  $120^\circ$  and facing downward  $45^\circ$  in order to be more efficient for up-going neutrino detection. The LCM is placed at the center of the frame (see fig. 2.4).

All the electronic commands, the clock signal, the slow control, the HV supply and the readout, arrive at the OMs via the electronic boards housed in the LCM. The main electronic board is the Analogue Ring Sampler (ARS), the ASIC chip used for signal processing and digitization (see section 3.2). The ARS provides the time and amplitude of the signal produced in the PMT, both of which are essential to reconstruct the muon track direction and estimate its energy.

## 2.4 The Line

ANTARES is composed by 12 lines (see fig. 2.5). Each line contains 25 storeys and has a length of  $\sim 450$  m. The lowest  $\sim 100$  m are not instrumented in order to avoid the fouling and the mud spread out from the seabed by the marine currents. The 25 storeys are 14.5 m equidistant and grouped in five sectors. In each sector, one particular LCM is called the Master Local Control Module (MLCM) which contains the Ethernet switch to concentrate the data traffic coming from the other 4 LCMs and from itself. The lines are anchored to the seabed by the Bottom String Socket (BSS), and held vertically by a buoy at the top of the line. In the BSS, there is the String Power Module (SPM), which provides the power supply to the BSS instruments and to all the LCMs in the string. The electronics required by the slow control system, the clock and the instruments of the BSS are contained in the

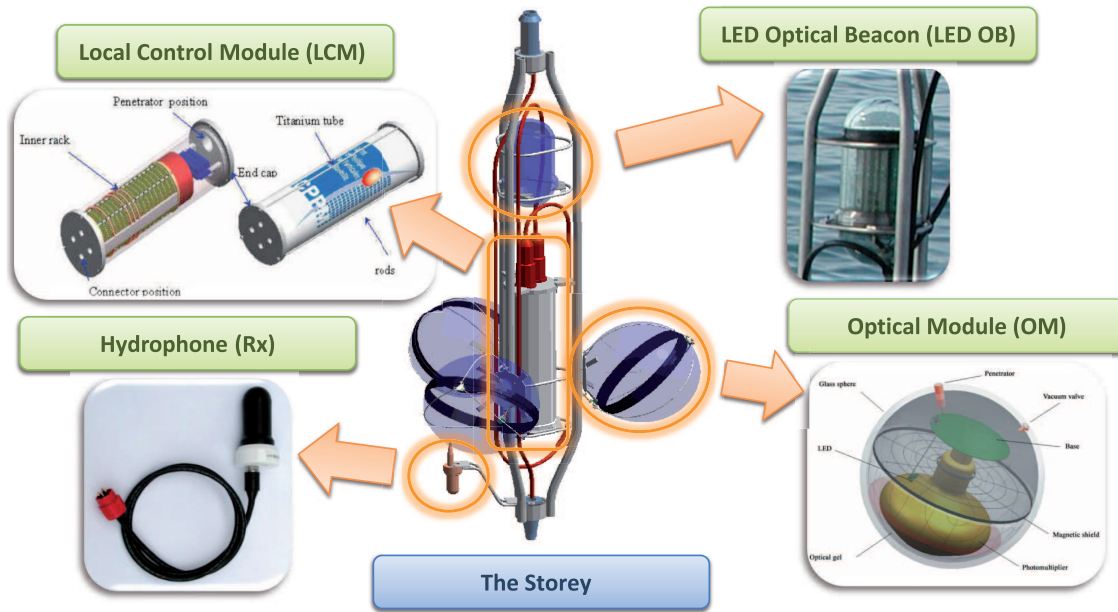


Figure 2.4: Scheme of one storey of the ANTARES detector.

String Control Module (SCM), which also takes care of the control of the data traffic from the MLCMs. The instruments in the BSS are an acoustic transponder RxTx hydrophone, a pressure sensor, and a sound velocimeter. In addition, the BSS of Lines 7 and 8 have a Laser Beacon for timing calibration.

Before the final integration of the lines, some mechanical tests were done with prototype lines as the Mini Instrumentation Line with Optical Modules (MILOM), where the OMs, the Optical Beacons, and some monitoring instruments were tested. A prototype line, the so-called Line 0, was deployed with the aim of studying the leak-tightness of the proposed electronics container scheme and the behaviour of the proposed design for the electromechanical cable. Line 0 also included a prototype of an acoustic detection system.

## 2.5 The Junction Box and the electro-optical cable

The connection between the shore station and the detector is made by the main electro-optical cable (MEOC) which is 42 km long. It has 58 mm of diameter and is composed of 48 monomode pure silica optical fibres. It is designed to provide all the electronic commands, clock, power supply, etc. This cable arrives up to the junction box, an egg-shaped vessel made up of titanium (see fig. 2.6) powered at 3700 V. The junction box (JB) splits the signals from the MEOC and distributes them to the lines by means of electro-optical interconnecting link cables. The signals from the junction box are received in the BSS of each line and are sent to the whole line.

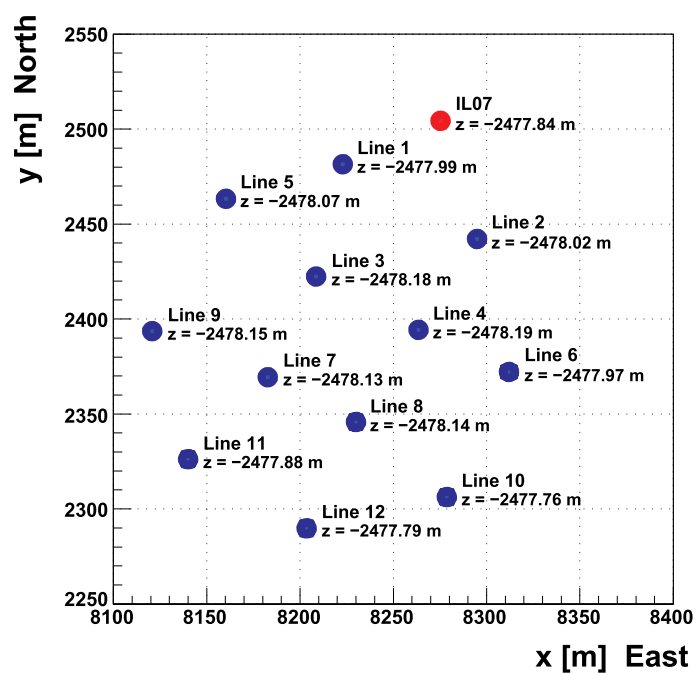


Figure 2.5: Position of the lines in the ANTARES Neutrino Telescope.

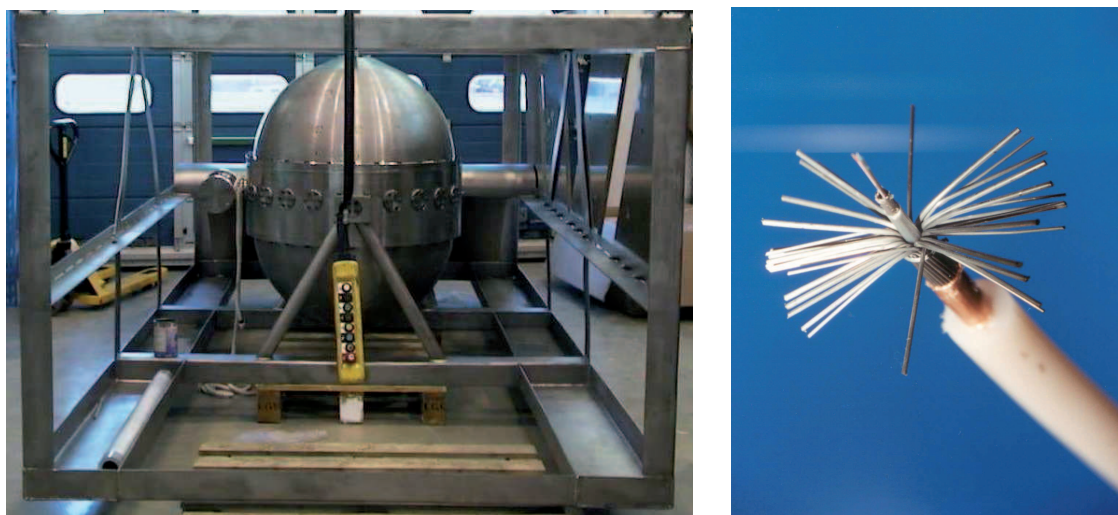


Figure 2.6: *left*: Picture of the junction box; *right*: picture of the main electro-optical cable open.



# Chapter 3

## Time calibration of the ANTARES detector

### 3.1 The ANTARES time calibration system

In ANTARES, the expected attainable angular resolution is better than  $0.3^\circ$  for  $E_\nu > 10$  TeV, as long as the positioning and the time calibration precision requirements ( $\sim 0.5$  ns in relative time resolution and  $\sim 10$  cm in positioning) are fulfilled.

Concerning the time calibration, we can distinguish between the absolute and the relative time resolution. The absolute time resolution corresponds to the ability of the detector to measure the time of each event with respect to the universal time (UT). This is necessary to obtain correlations with the physics phenomena (e.g. GRB, SN flares, etc.) The required accuracy is of the order of  $\sim 1$  ms. The main uncertainty for the absolute timing in ANTARES comes from the electronic path common to all the OMs. The MEOC, which links the junction box with the shore station, is the principal error source due to its length.

The relative time calibration is the ability of measuring the same time for an identical hit, not depending on which OM hit is recorded. In other words, to set a common reference for the whole detector. This is essential to achieve the best angular accuracy which is limited by the muon track reconstruction. In order to calibrate the detector, the time offsets of each OM due to its specific PMT transit time and the front-end electronics are measured. The main uncertainties contributing to the relative time resolution come from the transit time spread (TTS) of the signal in the PMTs which gives  $\sim 1.3$  ns of uncertainty, the optical properties of the sea water (light scattering and chromatic dispersion) which gives  $\sim 1.5$  ns of uncertainty for a distance of 40 m, and the electronics of the system. The later contribution is the only one which can be controlled, and in ANTARES it is required to contribute less than 0.5 ns to the overall relative time resolution, to reach the optimum angular resolution.

#### 3.1.1 On-shore dark room calibration system

In order to estimate the OM time offsets before the deployment of the lines, the integration sites of ANTARES (CPPM at Marseilles and CEA at Saclay) have assembled a calibration setup consisting in a laser ( $\lambda = 532$  nm) able to send very short (FWHM  $\sim 0.8$  ns) and intense ( $E \sim 1$   $\mu$ J) pulses of light to the PMTs through a system of optical fibres. The main purpose of this system is to compute the relative time offsets between the OM responses

and a synchronous laser signal whose emission time is measured by an internal photodiode. The time of the laser signal arriving at the OM is recorded by the ARS cards. Therefore, the individual PMT offset can be worked out after the correction of the time spent in the optical fibre path and the clock phase (the clock phase takes into account the different delays in the acquisition starting time depending on the storey and the line). The calibration is performed by sectors of five storeys. The light of the laser pass through an 1-to-16 splitter which provides a synchronous signal to the 15 OMs involved. Taking a particular ARS of a specific OM as a reference, the relative offsets can be inferred for the whole detector. In fact, for each line the ARS0 on OM0 is taken as the reference for the whole line. That gives a small inter-line time incertitude of the order of a single OM time offset. This small offset is corrected *in situ* by the Laser Optical Beacon.

### 3.1.2 The internal clock calibration system

Is a very precise time reference clock distribution system which consists of a 20 MHz clock generator on shore, a clock distribution system and a clock signal transceiver board placed in each LCM. A common clock signal is provided to the ARSs too (see section 3.2). This system includes an echo-based time calibration whereby each LCM clock electronics board is able to send back a return signal through the same optical path as the outgoing clock signals. This system enables the time offsets between all LCM clock boards to be measured by recording the propagation delays of the return signals of each storey with respect to the original clock signal emission time. Measurements in real conditions show a resolution of  $\sim 0.1$  ns, well within the specifications. The system also includes the synchronization with respect to Universal Time, by assigning the GPS timestamp to the data, with a precision of about 100 ns, much better than the required precision of  $\sim 1$  ms.

### 3.1.3 The internal Optical Module LEDs

Inside each Optical Module there is a blue LED attached to the back of the PMT capable of illuminating the photocathode. These LEDs are used to measure the relative variation of the PMT transit time and dedicated runs of this LED calibration system are customarily taken. This system is used to calibrate the path travelled by the signal starting at the PMT photocathode up to the read-out electronics. The effect of the transmission of the light in water is, however, not addressed by this calibration method.

### 3.1.4 The Optical Beacons

With the OB system [17] it is possible to illuminate each OM with a controlled time emission and compare the differences in the arrival times between them. The system consists in a series of pulsed light sources distributed throughout the detector. There are two kind of optical beacons: the LED Beacons and the Laser Beacons.

#### LED Optical Beacons

The LED Optical Beacon (LED OB) is a device made up by 36 individual blue LEDs ( $\lambda = 472$  nm) arranged in groups of six on six vertical boards, which are placed side by side forming an hexagonal cylinder. On each face, one LED points upwards and the rest point

radially outwards (see fig. 3.1). The 36 LEDs in the beacon can be flashed individually or in combination, and at different intensities (maximum intensity produces 160 pJ per pulse).

The faces are mechanically fixed to a hollow nylon structure which internally houses a small Hamamatsu H6780-03 photomultiplier tube, a photocathode of 8 mm diameter with a risetime of 0.8 ns and a transit time of 5.4 ns, used to provide the precise time of emission of the light flash independently of the triggering signal. A flat acrylic disc that acts as a lightguide is fixed to the upper part of the nylon mounting to increase the collection of light and a conical depression was machined in its centre, to direct light into the photomultiplier tube. The edges of the disc were also beveled at 45° to improve light collection from the horizontal LEDs.

There are placed 4 LED OB per line, in the floors 2, 9, 15 and 21, except in the line 12, where there is no OB in the floor 21. That configuration allows a time calibration inside the line by sections (see section 4.4.1). Presently, two OBs on floors 2 of lines 6 and 12 have been modified with respect to its original design, and have been equipped with some LEDs of different wavelengths to study the optical properties of the water and with new models of more powerful LEDs to make developments for the future telescope KM3NeT. Nevertheless, they are still suitable for time calibration.

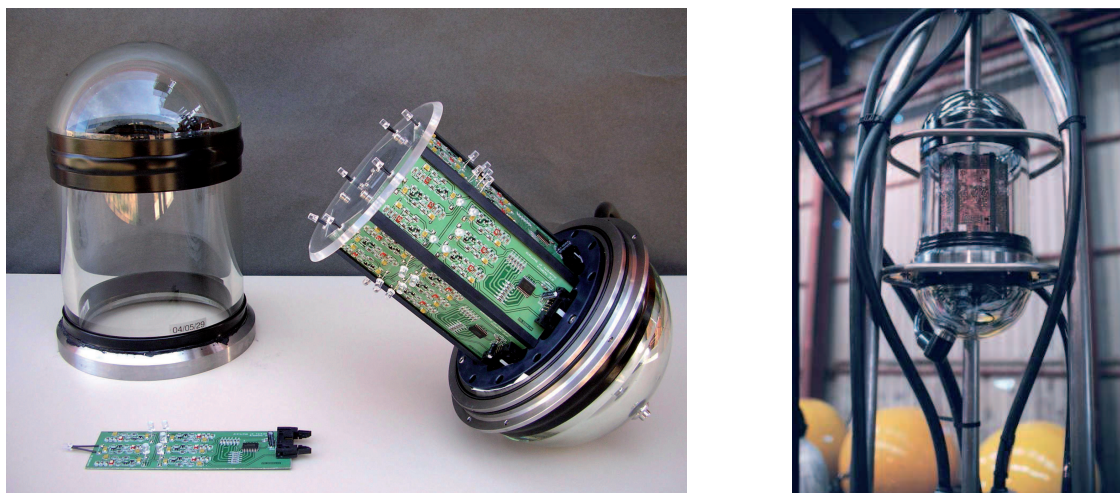


Figure 3.1: *left*, the LED OB without the upper cap of its borosilicate container. One of the board circuits is also shown; *right*, the LED OB installed in the storey frame.

### Laser Optical Beacon

The Laser Beacon is placed in the base of the line 8 and it has been designed mainly to perform the time calibration between lines (see section 4.5). Its main component is a diode pumped Q-switched Nd-YAG laser which produces short pulses with a time duration less than 1 ns (FWHM) and a total energy of  $\sim 1 \mu\text{J}$ . The model is a NG-10120-120 8 which emits at 532 nm after frequency doubling of the original Nd-YAG wavelength of 1064 nm. The actual time of laser emission is obtained thanks to a fast photodiode integrated into the laser head. Once the laser shot is produced, the built-in photodiode sends back a signal which is passed to an ARS chip located in the SCM.



Figure 3.2: *left*, the Laser OB and its titanium container; *right*, detail of the upper end-cap of the Laser OB with its antibiofouling quartz rod system.

The laser is housed in a cylindrical titanium container 705 mm in length and 170 mm in diameter (see fig. 3.2). The bottom endcap holds the penetrator of the cable connectors. Inside the container, an aluminium inner frame holds the laser and its associated electronics. The laser beam points upwards and leaves the container through an opening in the top end-cap. In this opening there is an optical diffuser comprising a flat disk diffuser with a thickness of 2.2 mm and a diameter of 25 mm that spreads light beam out following a cosine distribution, so that the light can reach the surrounding lines.

In order to minimize transmission losses due to underwater sedimentation and biofouling (the laser is more affected by this effect since it is pointing upwards), a quartz cylinder was bonded to the upper surface of the diffuser. The upper surface of this cylinder is coated with a black, water resistant epoxy layer. The light then leaves the cylinder through the vertical wall where biofouling is negligible. Due to Snells law, the cosine distribution is conserved when the light leaves the cylinder through its vertical wall. The dimensions of the cylinder were chosen to be 40 mm in diameter and 47 mm in length. These dimensions, together with the refractive index of quartz ( $n = 1.54$ ) and water ( $n = 1.34$ ) determine the maximum and minimum angle of the outgoing light, which were selected to maximize the number of storeys illuminated in the closest lines, while taking into account the technical constraints of the cylinder fixing due to the high pressure.

### 3.1.5 Down-going muon tracks

The thousands of down-going muon tracks detected per day also can be used as a cross-check of the overall space-time alignment and calibration by means of the hit time residual distributions of the reconstructed muon tracks.

## 3.2 Readout electronics: The ARS

The ARS [18] is the chip card in charge of measuring and processing the signal detected by the PMT. With the aim of reducing the dark-current noise of the PMT, an amplitude threshold (L0), whose typical value corresponds to 0.3 photo-electrons, is set. When this threshold is crossed, a time-stamp (TS) and a time to voltage converter (TVC) value are generated providing the time information. Simultaneously, the charge is integrated within a

gate of 35 ns long. The sampling frequency can be tuned between 150 MHz to 1 GHz. A Pulse Shape Discriminator (PSD) analyses the pulse shape classifying the signal as single photo-electron (SPE) or waveform (WF). Both WF and SPE modes provide the charge and the arrival time of the hit. In the WF mode, the analogue signal is sampled 128 times every  $\sim 1.6$  ns. This mode is very useful in order to do detailed analysis of the signals as calibration and timing parameter calculations. Nevertheless, it produces a big amount of data and currently, only SPE signals are recorded for physics analysis.

In a second step, the pulse information (SPE or WF), charge and time, is sent to a pipeline memory made up of 16 cells, which is able to handle 16 SPE hits or 4 WF hits. This process releases the ARS in order to acquire new hits without waiting for the precedent hit digitization. The hits in the pipeline memory are digitized by the Analogue to Digital Converters (ADC). The digital values for the charge (AVC) and time (TS + TVC) are generated for the selected hits and sent to the shore station. Afterwards, the pipeline memory is released and remains ready to process new events.

### 3.2.1 Time measurement

The time information of every hit is provided by the TS (concise time) and the TVC values (fine time). The TS gives the number of half clock cycles (25 ns) from the last reset time stamp (RTS). The TS is referred to the last RTS because the ARS has an internal clock which is reset every RTS. With the last RTS and the TS, it is possible to know the time from the beginning of the run of every recorded hit with an accuracy of 25 ns. Since the clock system is synchronized with the Universal Time, the absolute time can be obtained by assigning the GPS time to the data.

A higher precision is reached with the time to voltage converter (TVC) given by an 8-bit internal ADC in the ARS. This ADC provides a subdivision of the complete clock cycle (50 ns) in 256 parts, therefore, a precision of about 200 ps is attainable (see fig. 3.3). A ramp generator provides a voltage proportional to the time within a clock cycle duration. When a PMT signal crosses the L0 threshold, the ramp voltage is frozen and memorized providing the TVC value. Because of the dead time spent on recovering the ramp shape, a flip-flop system based on two TVC ramps is used.

In the ideal case, the TVC ramps would start synchronized with the clock cycles. However, there is a small shift between them. This effect has to be taken into account when computing the hit time, and the TS value has to be corrected to match the real time value.

The value of the TVC units is translated into time by:

$$t(ns) = 50 \times \frac{TVC - TVC_{min}}{TVC_{max} - TVC_{min}} \quad (3.1)$$

where  $TVC_{min}$  and  $TVC_{max}$  are the limits of the real dynamic range of the TVC. Ideally, the TVC range has 256 channels, but in the real case, only around 200 channels are available. The values of the  $TVC_{min}$  and  $TVC_{max}$  are obtained filling the TVC with a random flat distribution. Then, the  $TVC_{min}$  is defined as the first channel exceeding the 10 % of the average occupancy, and the  $TVC_{max}$  is the last one exceeding this 10 % average occupancy.

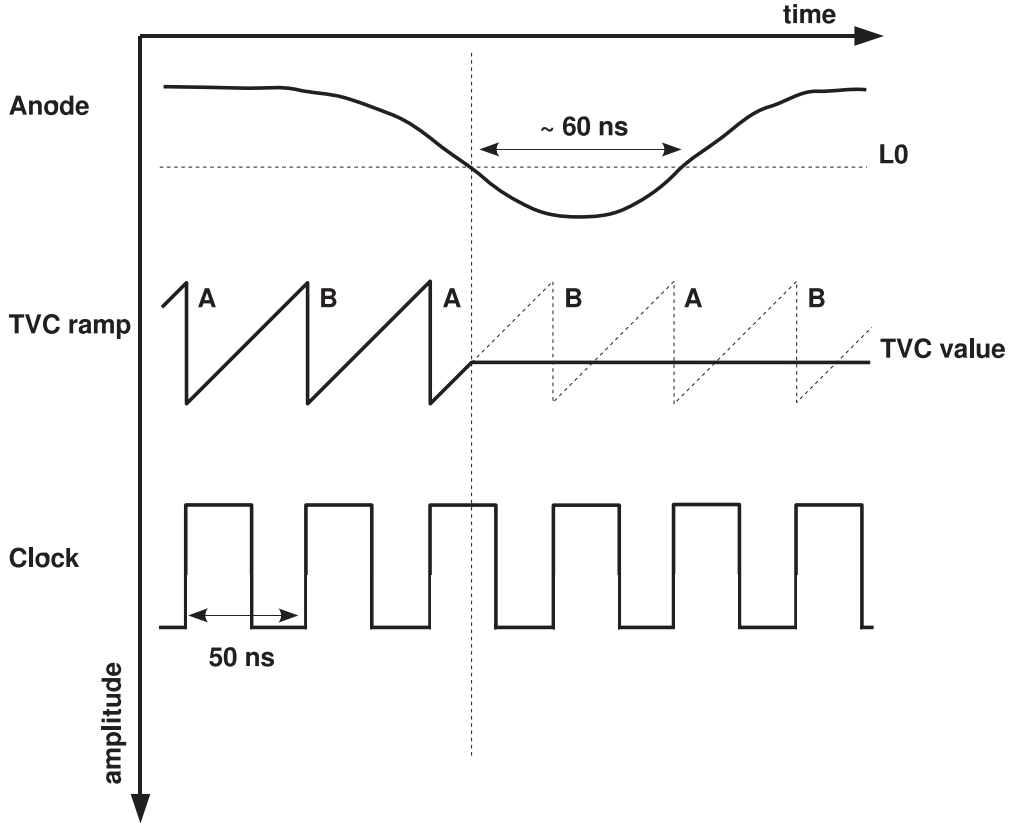


Figure 3.3: Time measurement procedure in the ARS. A time stamp and a TVC value are generated when the signal crosses the L0 threshold.

### 3.2.2 Charge measurement

The PMTs have a nominal gain of  $5 \times 10^7$  which gives, for a single photo-electron collected in the PMT anode, a signal of about 45 mV ( $50 \Omega$  load). The charge integration is carried out in three steps in order not to lose any charge. This is done by means of three capacitors working in three different phases (see fig. 3.4): the integration phase (I), where the signal from the anode is integrated, the memorization phase (M), where the integrated charge is recorded in memory, and the charge erasing phase (R), where a reset is done. These phases have an adjustable time cycle duration between 8 and 30 ns, which is on purpose slightly longer than the PMT rise time (defined as the elapsed time between the 10 % and the 90 % of the amplitude signal, around  $\sim 5$  ns). When a hit crosses the L0 threshold, the time integration is increased in order to cover all the signal pulse shape. This phase's duration is set between 17 to 50 ns. The charge integrated value is obtained as the sum of the two capacitors in the integration and memorization phase.

After this process, the integrated charge is digitized by an 8-bit ADC called analog to voltage converter (AVC) which provides values from 0 to 255. The conversion from AVC units to charge units (in photo-electrons) has been computed in the laboratory for each specific ARS. The results show that the AVC-charge relation can be considered linear:

$$Q_{pe} = \frac{AVC - AVC_0}{AVC_1 - AVC_0} \quad (3.2)$$

where  $AVC_0$  is the position of the pedestal and  $AVC_1$  is the position of the one photo-

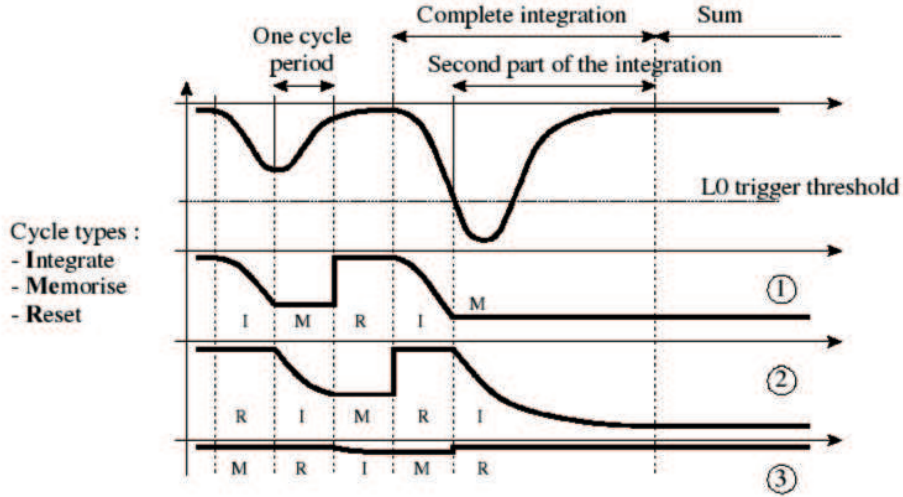


Figure 3.4: Charge signal integration with 3 capacitors working in different phases. When the L0 is crossed, the ramp voltage is frozen and memorized.

electron peak. The  $AVC\_1$  and  $AVC\_0$  values are calculated for each ARS, and stored in the ANTARES database. The values obtained show important differences among ARSs.

A second order correction known as “cross-talk” effect was found due to the influence of the TVC ramp values in the analog memory of the AVC during the ARS signal digitization (the reciprocal effect, i.e., TVC affected by the AVC, has not been observed). Different AVC values are found for the same charge input depending on the TVC value. This effect increases linearly with the TVC values.

The correction is typically of 4 channels for the complete TVC range. The linear correction to that effect can be written as:

$$AVC_{corr} = AVC - XT\_slope(TVC - TVC\_mean) \quad (3.3)$$

where  $XT\_slope$  is the slope (avc bit/tvc bit) of the linear cross-talk effect, and  $TVC\_mean$  is the centre of the TVC ramp  $((TVC_{max} - TVC_{min})/2)$ , where no cross-talk correction is needed, by definition.

In order to obtain the correct value of the charge, the  $AVC_{corr}$  value obtained in the equation 3.3 should be used as input (AVC parameter) in the equation 3.2. The expected relative error in the hit charge measurement is smaller than 10 %.

### 3.3 Effects to consider in the signal processing

There are several known effects that can modify the way the hit time is measured, the number of photons that are detected or simply the behaviour of the hardware in the signal. Those are well known and can be corrected or avoided in the analysis of the time signal used for time calibration.

### 3.3.1 Early-photon effect

The region where the PMT receives in average more than 1 photon per flash of the OB is called the “*early-photon region*”. The “*early-photon effect*” is a consequence of the inability of the PMTs to resolve multiple photons arriving from the same LED OB flash very close in time. Due to the big amount of light emitted by the LED OB, the PMTs next to the beacon record the time of the first arriving photons of the LED OB pulse. For the most distant PMTs, this effect disappears completely in the so-called “*photo-electron level region*”, where less than one photon per flash in average is detected (see fig. 3.5). The early-photon effect makes then a distinction between two different zones where different methods for time calibration should be applied. In fig. 3.5 the early-photon effect has been reproduced by a toy Monte Carlo. On the left several time residual distributions at different distances (15, 90, 165 and 240 m) between the OB and the OM are shown. The nearer the OM to the OB, the earlier and narrower the time residual distribution. The mean value of the time residual distributions versus distance are shown on the right part of the same figure, where the two regions, early-photon and photo-electron, are clearly distinguished.

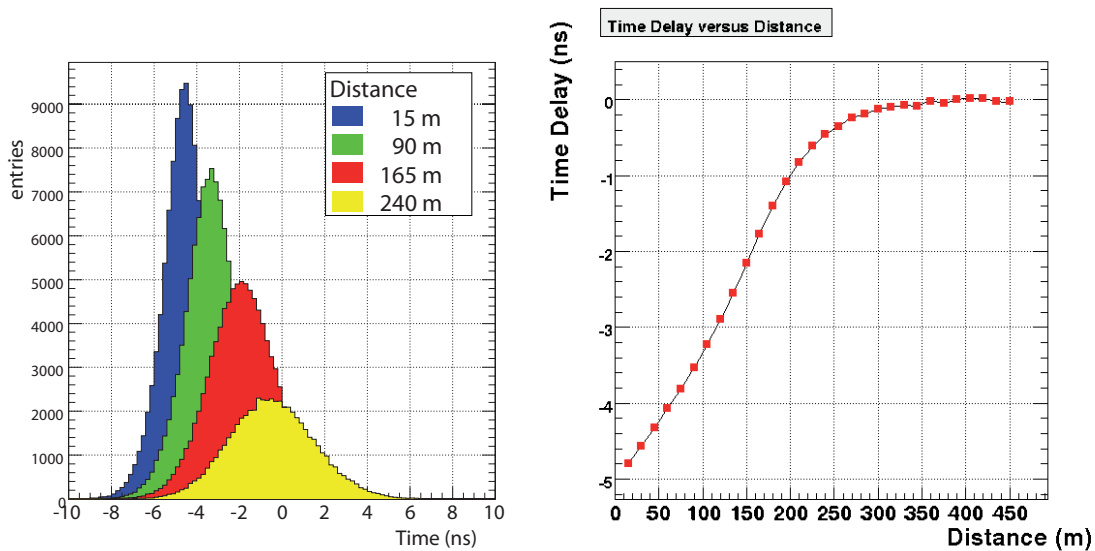


Figure 3.5: *left*: Arrival time distributions for different distances between the OB and the OM; *right*: Projection of the mean values of the time distributions as a function of the distance. The two regions: early-photon and photo-electron region are clearly visible.

### 3.3.2 Walk effect

Two events which are supposed to arrive to the OMs simultaneously may not produce the same time-stamp because of their analog signals are different in amplitude. Being the discriminator threshold fixed (L0 threshold), the largest signal will cross the threshold before the smallest one. This effect is known as “*walk effect*” (see fig. 3.6) and is currently corrected using the charge produced in the hit.

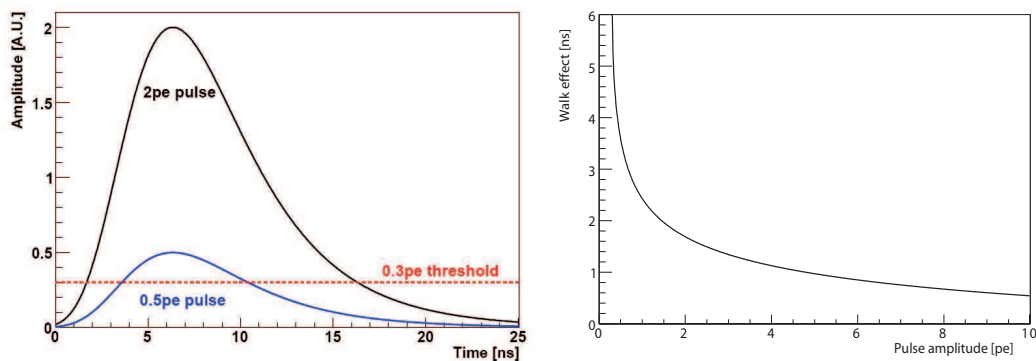


Figure 3.6: *left*: A schematic picture of the walk effect. The biggest the signal the sooner it crosses the discriminator threshold; *right*: A graph showing the recorded ARS time as a function of the hit signal amplitude recorded by the PMT.

### 3.3.3 DNL effect

In the equation 3.1 it was assumed that all the TVC channels are identically wide. However, it is well known that they are different in size and the channels of the internal ADC of the ARS that stamps the TVC have a non uniform answer. This unequal binning is called Differential Non Linearity (DNL) and has a non-negligible influence on the time measurements. The time size of each channel differs from one to each other, giving to some time values, inside the same time stamp, more chances to be selected for the TVC (see fig. 3.7). Because of that, what should be a Gaussian peak signal is deformed in several peaks. The results show a small effect in such a way that, without correcting by the DNL effect, the error on the TVC measurements is around 0.3 ns (depending on the ARS chip) and once DNLs are corrected, the error is around 0.09 ns. This second order correction is not, at the moment, taken into account in the ANTARES time measurement. This problem can be avoided with a correct choice of the size of the bin. However, studies to understand and correct the effect are ongoing.

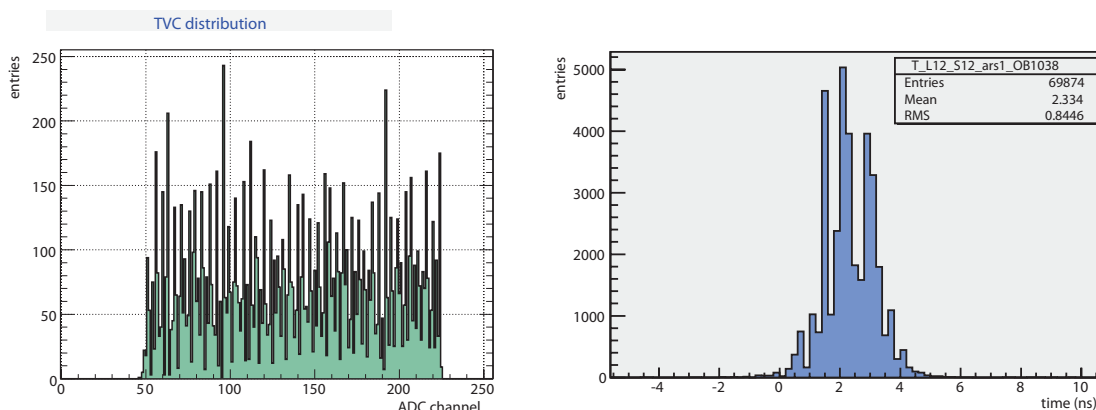


Figure 3.7: *left*: Response of the 256 TVC channels under an uniform signal. The differences on the bin contents are due to the DNL; *right*: Example of various peaks due to the DNLs in the ARS 1 of the floor 12 of line 12, flashed from the LED OB from the floor 9 of the same line. The effects of the DNL are clearly visible.

### 3.3.4 Token Ring effect

There are two ARSs per PMT. A *token ring* protocol is used to chain the two ARS chips serving the same OM, in order to decrease the acquisition dead time. Each ARS includes a register named “*token*”. If the token is set to 1, the ARS owns the token and will treat the incoming events. Otherwise it will ignore them. At any time one and only one ARS should own the token. The token is passed from one ARS to the other with a delay of about 10-20 ns after the end of the integration gate.

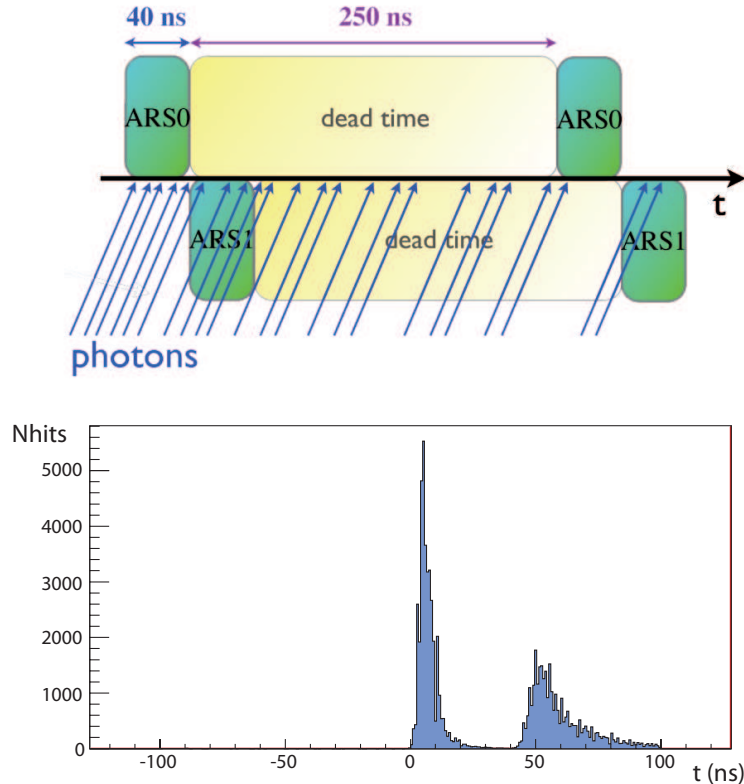


Figure 3.8: *up*: Scheme of the working process of the ARS pair of an OM; *down*: Example of a typical time residual distribution in ANTARES, of the ARS 1 (OM0) of floor 12 in line 12 flashed from floor 9 in line 12, with the time computation of the arrival hits. The second peak is due to the token ring effect.

Each ARS is connected to the other one and they pass the token between them with a protocol depending on the availability of the chips and on the status of event, i.e. hit, processing. So the pair of ARSs works as follows (see fig. 3.8): when the PMT receives a photon hit, the first ARS starts to integrate the signal until 40 ns. Then it passes the token to the second ARS, and wait until the next hit occurs in the PMT. If there is a high ratio of hits, both ARS cover the first 80 ns and the effective dead time is of 210 ns (250 ns of dead time minus the 40 ns of relieve of the second ARS) until they can process a hit again. When the ratio of photons per flash is greater than unit one of the ARS of the OM, after being busy during 40 ns processing the first hit, releases the token to the other ARS which starts to process the next hits that will accumulate as a second peak  $\sim 40$  ns after the first one (see fig. 3.8 down).

# Chapter 4

## Time calibration with the Optical Beacon System

### 4.1 Introduction

Although the detector is calibrated on shore on a dark room previously to the deployment, during the transport and deployment the different parts of the detector suffer stress and changes of temperature and pressure, which may deteriorate slightly the time calibration of all the system, not ensuring then the required time calibration accuracy for a neutrino telescope. Therefore, an in-situ measurement of the time offsets is needed to validate and monitor the values measured in the dark room, and in case of miscalibration, to apply the corresponding corrections. This is done with the Optical Beacon system which has been described on section 3.1.4.

Therefore, before making any physics analysis it is necessary to compute the calibration constants of the detector. Concerning time calibration, the parameters needed are the ARS\_T0 values, or also named the T0 values. This parameter is defined as the sum of the ARS offset and the clock phase of its corresponding storey. The computation of the T0 values is made from the time residuals distributions defined as the difference between the emission time of the OB light and the time recorded by the OM when the flash arrives. This quantity is corrected by the time spent by the light to reach the OMs:

$$T^{100} = t_{OM} - t_{OB} - \frac{d(OB, OM)}{c_{water}} \quad (4.1)$$

where  $t_{OM}$  and  $t_{OB}$  are the time recorded by the ARS reading the OM and the OB respectively,  $d(OB, OM)$  is the distance between the OB and the OM, and  $c_{water}$  is the speed of light in water. Once corrected, the  $T^{100}$  value should be equal to zero, any deviation from zero should be understood as a time offset not considered. However, there are some effects that should be taken in consideration for a correct understanding of the measured time (see section 3.3). For further information about the time calibration of the ANTARES detector see [19], [20] and [21].

### 4.2 Previous calibration procedure

When the OMs are flashed by the OB system, the emission time of the flash and the arrival time of the hits to the OMs are digitized by the front-end electronics and sent to the shore to

be processed and stored on disk for later analysis. The optical beacon flashes are previously programmed via special calibration run setups designed to perform the time calibration with the optical beacon system. As soon as a calibration run is performed, the arrival times of the emission flashes and the OM hits stored in the calibration run files are processed to obtain the time residual distribution of each ARS according to the equation 4.1. One example of such distributions can be shown on figure 3.8, where the two peaks due to the token ring effect (see section 3.3.4) are visible. The aim is to obtain the time corresponding to the peak of these distribution, i.e. the  $T^{100}$  value. The  $T^{100}$  value is obtained fitting the time residual distribution to a Gaussian or to the convolution of a Gaussian and an exponential. The selection of the fit function depends on the distance between the OB and the OM. For OMs near to the OB, the photons have not suffered too much scattering so the shape of the distribution is almost Gaussian, whereas for further OMs the presence of more scattered photons produces a tail in the distribution and a fit to the convolution of a Gaussian and an exponential is more appropriated (see fig. 4.1).

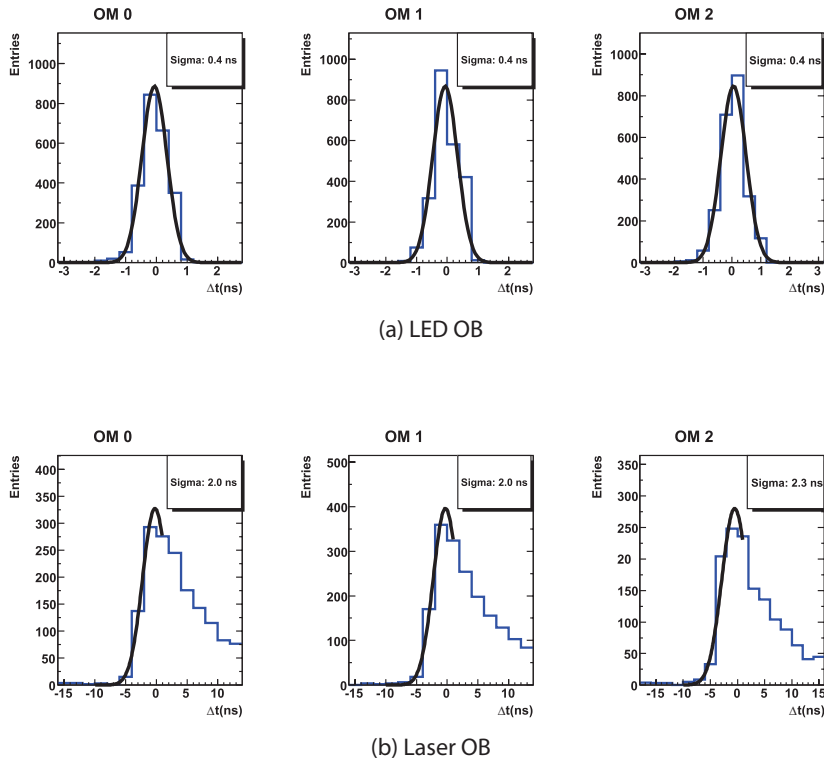


Figure 4.1: Example of a typical time distribution fitted from a close LED OB (*up*) and from the distant Laser OB (*down*).

The mean value is computed after a special fit procedure which is done in two steps. The first step consists of a Gaussian fit from the bin with 20 % of the maximum occupancy to the bin with 100 %. Then, a second fit is performed taking as reference the mean value of the previous fit. This second fit goes from the bin with 10 % of the mean value bin occupancy to the one having a 85 % occupancy after the mean. The  $T^{100}$  value to use for time calibration is the maximum of the fitted function.

### 4.3 Automation of the time calibration procedures

An appropriate bin size for the fit, big enough in order to avoid the DNL effect but not too wide to avoid a loss in the time precision, should be chosen. To find that compromise is not easy. In the previous method, the size of the bin was manually chosen depending on how the distributions were affected by the DNL and by the scattering of the photons which basically is a function of the OB-OM distance. Some  $T^{100}$  values obtained in this way shows a major deviation which usually was not due to a miscalibration but to a failed fit. That implies a visual inspection of all the fits were the T0s are too much deviated in order to disentangle if the deviation is due to a failed fit or due to a bad choice of the bin size. In the latter case the bin size is modified manually and the fit is repeated again. This manual procedure for the nearly 1800 ARSs of the detector takes around 2 weeks of dedicated hard work, which together with the need of recalibrating the detector every tuning of the high voltage used in the PMTs, line repairs or redeployments, or simply by fortuitous miscalibration with time, made imperative to find a better way to calibrate the ARSs.

With this idea in mind, an automate method has been developed which aims is not only to avoid the necessity of revision and refitting of the time differences distributions, but also to make it fast and easy to perform, with the less human intervention needed as possible, and obtaining as good results as with the previous method.

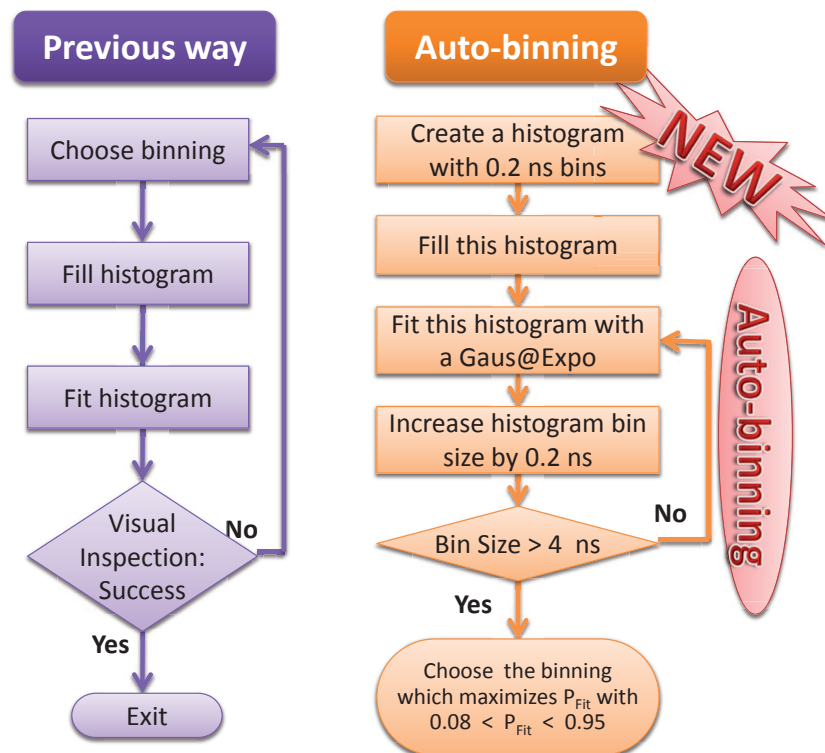


Figure 4.2: Flux diagrams showing the “previous way” time calibration method to obtain the  $T^{100}$  values, left, and the “auto-binning” method, right.

### 4.3.1 Auto-binning: increasing the chances to have a good fit

The auto-binning procedure consists in an algorithm which tries to find the best bin size to perform the fit of the residual time OB-OM distributions. The main difference with respect to the previous way (see fig. 4.2) is that the bin size is varied automatically until the most optimum one is found. The automatic algorithm starts building a time difference distribution histogram with a bin size of 0.2 ns. Then, the distribution is fitted to a Gaussian function convolved with an exponential:

$$f(t) = \frac{A}{\sqrt{2\pi\sigma^2}} e^{-\frac{(t-\mu)^2}{2\sigma^2}} \otimes e^{-\lambda t} = \frac{A}{2\lambda} e^{\frac{\sigma^2}{2\lambda^2}} e^{-\frac{(t-\mu)}{\lambda}} \left( 1 + \operatorname{erf} \left( \frac{\lambda(t-\mu) - \sigma^2}{\sqrt{2}\lambda\sigma} \right) \right) \quad (4.2)$$

where  $A$  (amplitude),  $\mu$  (mean of the Gaussian),  $\sigma$  (sigma of the Gaussian) and  $\lambda$  (decay constant of the exponential part) are the parameters of the fit function. This is done two times: a first fit is done with a rough situation of the parameters of the fit. The output parameters of this fit are used as initial parameters of the second fit. The function in the equation 4.2 has the advantage to fit very well the shapes of the measured time residual distributions (see fig. 4.3). The range of the fit is chosen in the following way:

- The lower limit of the fit is chosen as the bin whose content is lower than the 5 % (20 % for the first fit) with respect to the bin with the maximum content (BWMC) and to the left of the peak.
- The upper limit of the fit is chosen as the bin to the right of the peak whose content is lower than the 5 % (20 % for the first fit) of the BWMC.

Sometimes the tail of the distribution does not reach the 5 % in the time window defined by the limits of the histograms. As it has already been mentioned in the section 3.3.4, due to the token ring system and the dead time of the ARS, a second peak may appear. In this case, the upper limit of the fit is defined as the time of the BWMC plus the 20 % (15 % for the first fit) of the distance between the BWMC and the minimum between the BWMC and the second peak due to the token ring effect. The way to find the minimum between the two peaks is the following: the histogram is rebinned, increasing the bin size to avoid the fluctuations due to the DNLs, until only two local maximums (two peaks) appear in the histogram. Then, the bin with the minimum counts between both maximum peaks is taken as the minimum between them.

Once the fit is performed, the  $P(\chi^2)$  of the fit is checked and if lies in the range  $8 \% < P(\chi^2) < 95 \%$  the fit is considered good enough and chosen as the final fit for that ARS. If not, the bin size is increased in 0.2 ns steps and fitted again, until the previous condition is given or until a bin size of 4 ns is reached. If finally, the fit is made with a 4 ns bin size but the  $8 \% < P(\chi^2) < 95 \%$  condition is not satisfied, the fit with the highest  $P(\chi^2)$  is chosen. This method converges very fast to obtain the  $T^{100}$  values and is quite stable.

### 4.3.2 Fit quality tagging and fast visual cross-checks

Despite all these improvements, sometimes there is no signal available or it has been distorted by other reasons. To avoid the use of bad fits in the time calibration, because of bad quality

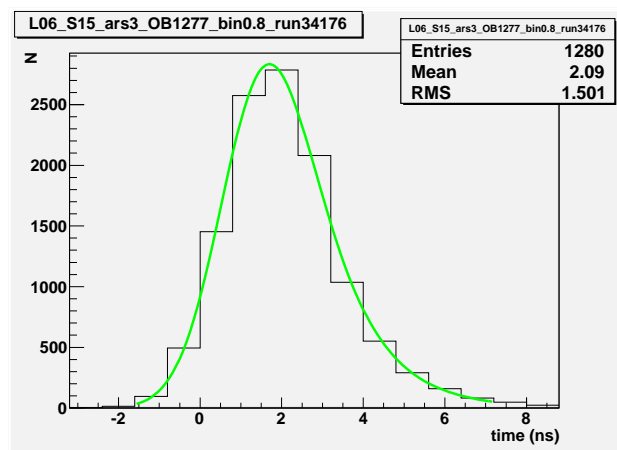


Figure 4.3: Example of a time residual distribution fitted to a Gaussian function convolved with an exponential. The distribution corresponds to one of the ARSs of the OM0 in the floor 15 of line 6, flashed by the LED OB of the floor 9 in line 10.

signals, depending on the quality of the final fit, an automatic classification of the time residual distributions is made which makes easier to decide if they are suitable or not for time calibration. A code based on automatic consecutive checks has been established to mark the fits with a control quality stamp(see fig. 4.4):

1. **GREEN (BLUE) CODE:** If the fit is not classified with one of the color codes described next, the fit is considered suitable for time calibration, and the color code is green. On the other hand, if the average number of hits per flash is greater than 1 then the colour code is BLUE: that means that the OM is in the early-photon region, receiving more than 1 photon per flash, the signal still is suitable for time calibration but has to be treated in a different way, so is tagged this way for future considerations.
2. **PURPLE CODE:** If the angle OM-OB is bigger than  $120^\circ$ . Then the OM can not receive direct light from the OB and the distributions are hard to be fitted.
3. **BROWN CODE:** If the average number of hits per flash is below 0.01 (1 %). When the OM is too far from the OB or is damaged the signal is mainly noise.
4. **RED CODE:** If the bin with the maximum content has less than 50 hits. This is a clue of an histogram with low statistics, surely because a faulty PMT or ARS.
5. **CYAN CODE:** If the bin with maximum content and the maximum amplitude of the fitted function differ more than a 75 %. If that happens most likely the fit has failed in the attempt to adopt the shape of the signal or simply the signal is useless for time calibration.
6. **YELLOW CODE:** If the fitted range is greater than 50 ns. Sometimes the signal is distorted because a shadowing effect or a non direct illumination. This condition prevents to use for time calibration non suitable  $T^{100}$  value.

With all this treatment, the obtained  $T^{100}$  values, the fit results and the conditions are stored together with a visual cross-check with the previous colour code to check easily the fits that passed the quality control defined above (see fig. 4.5). A total of 59 graphics showing

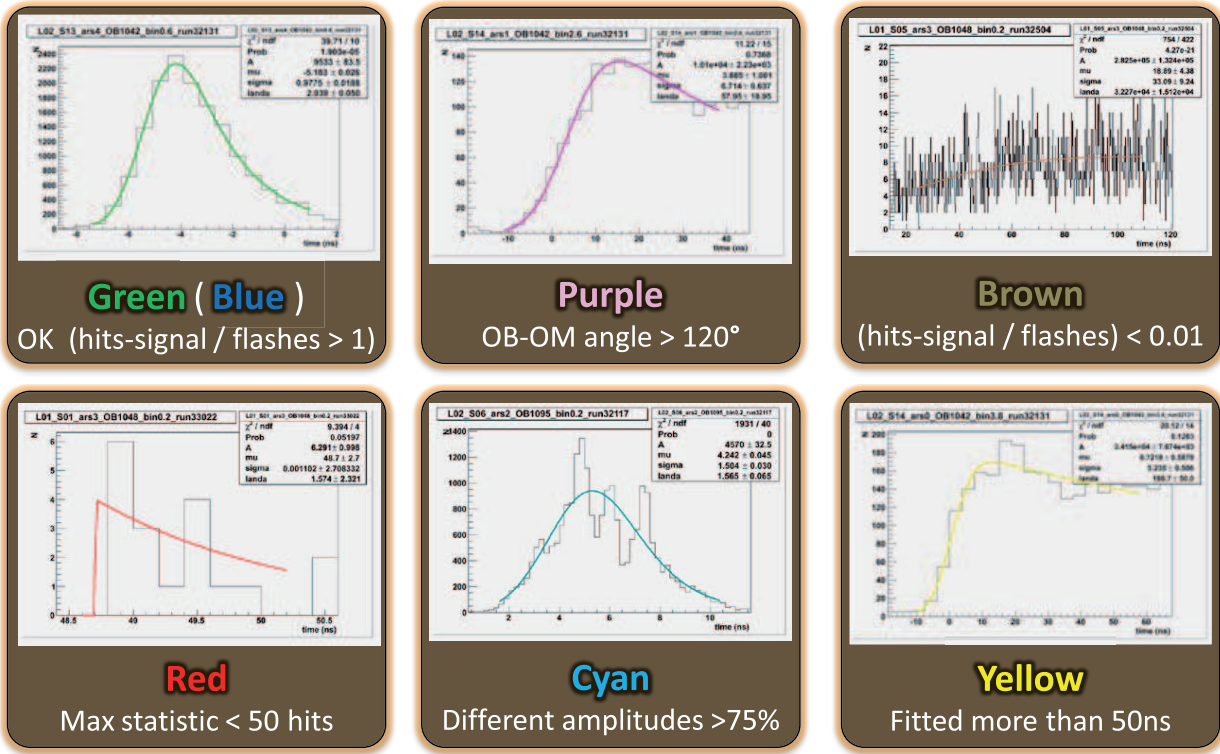


Figure 4.4: Colour code used for the fast visual cross-check of the auto-binning.

the final fits with their colour codes are produced, one per each sector of the 12 lines (5 sectors per line, minus the last sector of line 12 that has no OM triplets).

Once all the  $T^{100}$  values have been obtained and their conditions are stored, it is possible to start the time calibration calculation, alerting of the use of the bad fitted ones which are marked for a posterior analysis.

All the output of this automatic calibration procedure information is combined together with the data stored in the data base of the detector concerning the available OMs and dead channels for that calibration run. This information is taken into account when analyzing the  $T^{100}$  values marked for inspection. This makes that the process would be really an automate procedure.

## 4.4 Intraline calibration

The time calibration of the ANTARES detector is performed in two steps. The first one consists in the calibration of all the OMs of the same line (*intraline calibration*) and the second one consists in the synchronization in time of all the lines (*interline calibration*).

The intraline calibration aims to assure that the T0s of all the ARS of the same line are calibrated with respect to a particular OM used as reference. This calibration is performed by sections in such a way that each LED OB is used to calibrate the OMs of the upper floors that are facing down the OB: the LED OB located in the floor 2 is used to calibrate all the

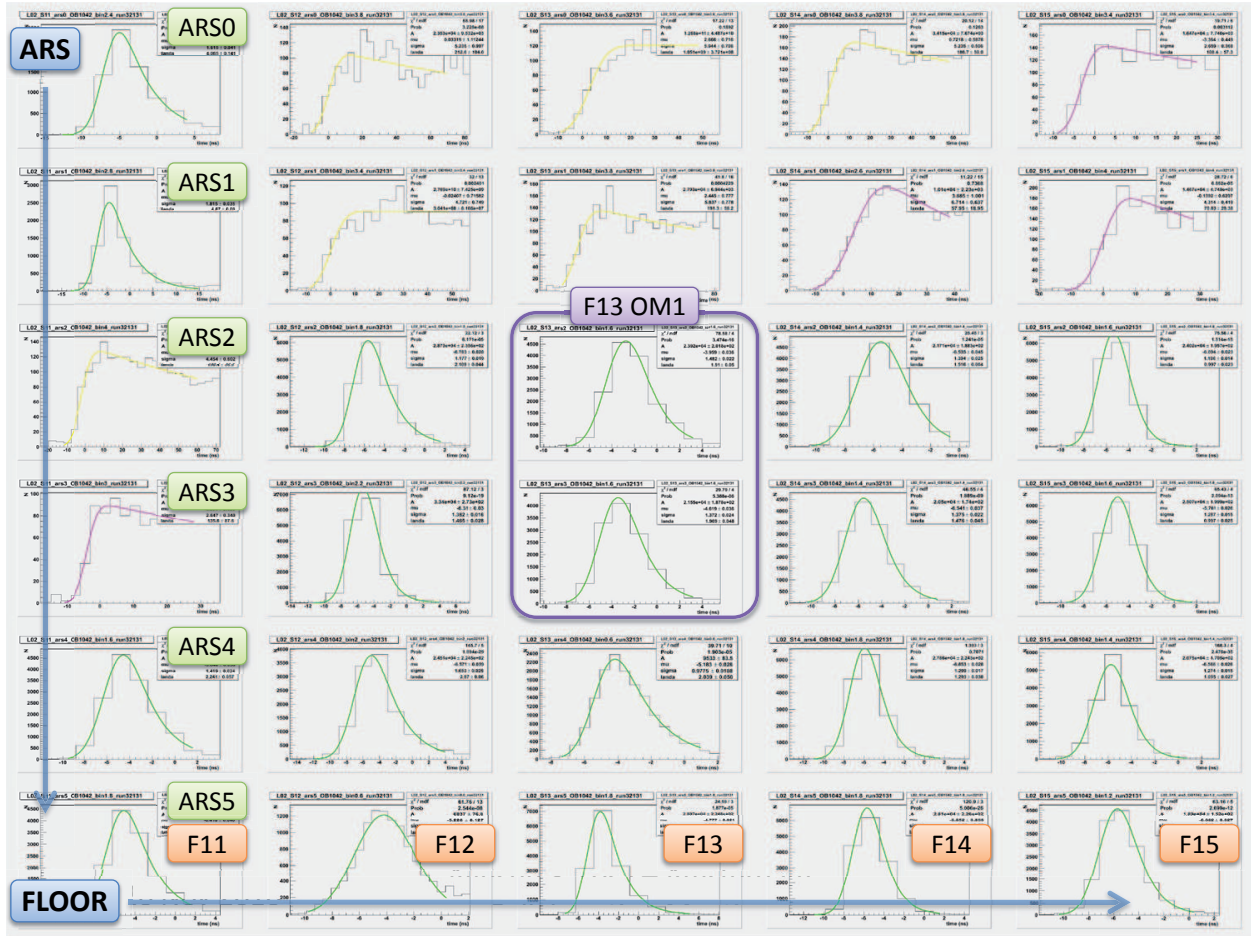


Figure 4.5: Example of a visual cross-check of the auto-binning procedure.

ARSs from floor 4 to 10 (*section #1*), with the LED OB located in the floor 9 the OMs from floor 11 to 16 are calibrated (*section #2*), with the LED OB located in the floor 15 are calibrated the OMs from floor 17 to 22 (*section #3*) and finally, with the LED OB located in the floor 21 OMs from floor 23 to 25 are calibrated (*section #4*). The floor 3 is too close to the OB of the floor 2 to be calibrated and the floors 1 and 2 are below the LED OB with no chance to receive direct light. Nevertheless, studies are ongoing about how to calibrate these first floors (*section #0*) with OBs of adjacent lines or with the Laser Beacon.

#### 4.4.1 Calibration by sections

Intraline calibration is made by sections and always in the so-called early-photon region, where a linear dependence of the T0s vs distance has been found. The mean values of the time residual distributions of the OMs in a given section are not centered at zero but, on the contrary, they show an additional delay that increases with the distance due to the early-photon effect (see section 3.3.1). This effect is reproduced in all the sections of all the lines being the slopes of the different fits to a linear law quite similar. The average value of the slope is 0.09 ns/m. Since this effect seems to be stable through all the detector, the deviations of each ARS from the fitted straight line will be used as the corrections to be applied to the T0 values measured on-shore in the dark room.

The calibration is done in the following way. For each section, a linear fit of the T0 values obtained from the time residual distributions as a function of the distance is made. If a T0 lies 2 ns further from the fit function, the ARS is removed and the fit is repeated again without the point corresponding to this ARS. This is done in an iterative way until all the T0 values included in the fit lie in the  $\pm 2$  ns region around the line fit (see fig. 4.6 and Appendix A). Then, after checking that all the excluded ARSs have been removed because they are miscalibrated and not because an incorrect fit in the automate calibration procedure (color code different from blue or green), the correction to be applied is the time distance from the T0 values to the final fit obtained by this way. This last check has been reduced considerably with the auto-binning method being most of the excluded points miscalibrated points and not the result of a bad quality fit.

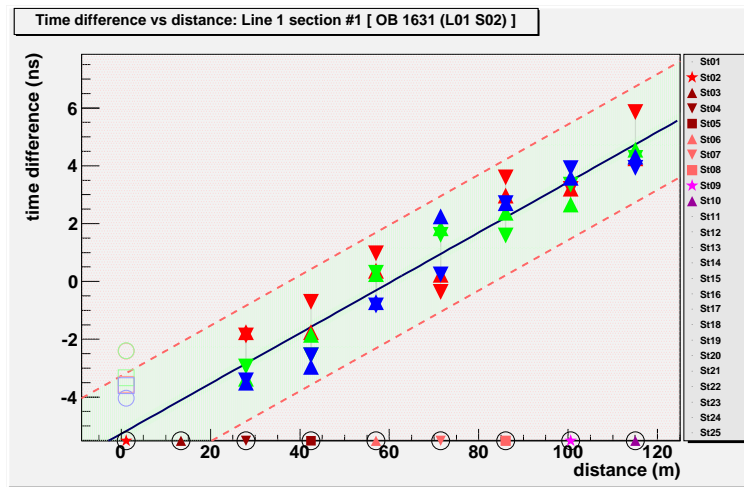


Figure 4.6: Example of the intraline calibration of the *section #1* of the line 1.

To be sure that the automate method gives at least the same precision in the time corrections than the “previous calibration method” they have been compared for a given set of corrections. Figure 4.7 shows the distribution of the differences between the T0s with the new method and the previous method. The RMS of the distribution is 0.4 ns indicating a good correspondence between both methods. Only 24 out of 914 corrections applied differ in more than 1 ns.

#### 4.4.2 Calibrating the first floors: Laser-OB and LED-OB

Until now, the first floors have not been easily calibrated because of the absence of an OB below them. One of the recent studies about how to calibrate these OBs systematically lies in the use of the real time positioning of the detector, which gives the possibility to measure the real OB-OM distances from different lines, to be used in the correction by the distance in the equation 4.1.

The difference with respect to the calibration performed in the other sections is that in this case the calibration can not be done in the early-photon region but in the photo-electron level region. The calibration method would be similar to the one made in the early-photon region but now the fit is done to an horizontal straight line. Again, the fit is done iteratively

excluding the ARSs which are 2 ns further from the line fit. For that purpose we can use the LED OB of the floor 2 of an adjacent line or the Laser OB if the first floors of the line are in the photo-electron level region (using the closest available in time Laser OB calibration run). As an example the calibration of the *section 0* of line 1 with the Laser OB and with the LED OB of line 2 are shown on fig. 4.8 and 4.9 respectively. Both methods and other possible combinations are presently being studied.

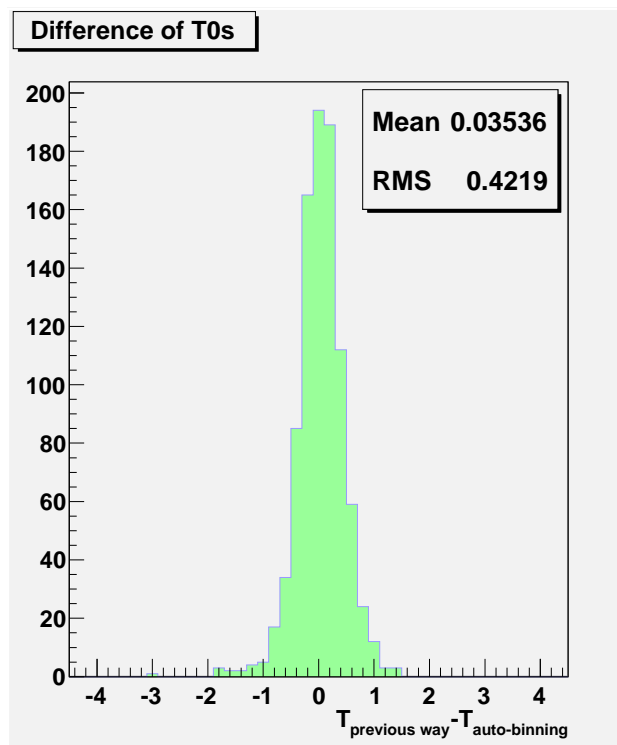


Figure 4.7: Distribution of the differences in the corrections to the T0s computed by the previous method and the ones computed with the auto-binning method.

## 4.5 Interline calibration

Once all the ARSs of all the lines have been calibrated, a possible time offset between lines could remain. The measurement of these offsets is the last step for a total time calibration of the detector. This last calibration can be performed with different OBs.

### 4.5.1 Laser OB

Until now the line offsets have been measured using the Laser OB located in the BSS of line 8. This beacon has enough power to illuminate all the lines until the photo-electron level region, giving a common frame to compare the collection of the time differences measured for each line. In this way, the T0s values of all the illuminated floors in the photo-electron level region of each line are fitted to a constant (see fig. 4.11 and Appendix B). The differences between lines are the real offsets between lines and, therefore, the T0s corrections necessary to finish the time calibration of the detector. In this case, the real positioning alignment is used. For a given period of interest, all the Laser OB calibration runs (usually one per

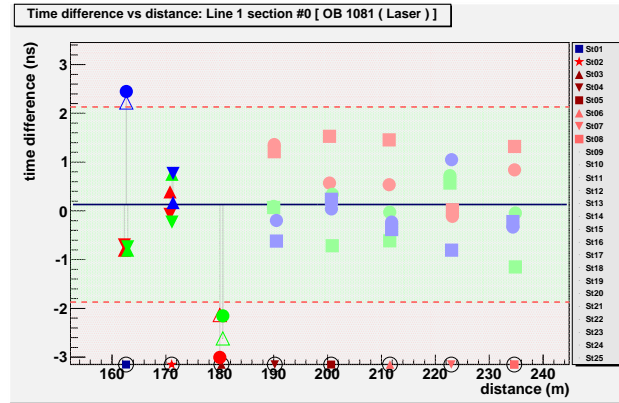


Figure 4.8: Example of the intraline calibration of the *section #0* of the line 1 by the Laser OB.

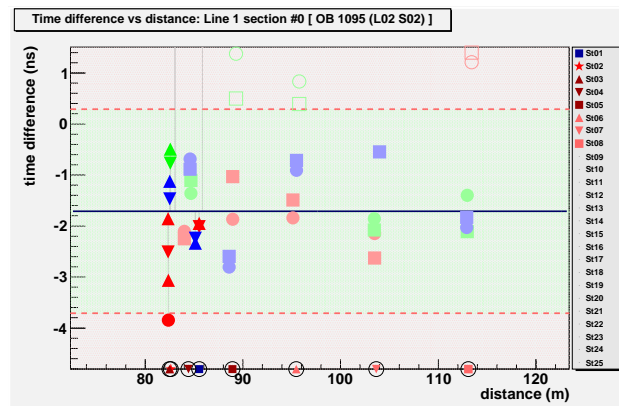


Figure 4.9: Example of the intraline calibration of the *section #0* of the line 1 by the LED OB of the floor 2 in line 2.

week) are analyzed. Currently, the study of the evolution in time of the line offsets along the period of Laser OB calibration is included. As it can be seen in the fig. 4.11 and in the Appendix B a great stability in time is shown.

Again, to be sure that the automate method provides the same precision in the time corrections than the previous calibration method, they have been compared for a given set of line offsets (see fig. 4.10), showing a good correspondence between them. The table with the line offsets values obtained by the previous method and the ones computed with the auto-binning method for the period of 10 lines of the ANTARES detector (line 4 was not available for that period), made with 12 Laser calibration runs from 25/02/2008 to 12/05/2008, is also shown.

## 4.5.2 LED OB

An analysis studying the possibility to use the LED OB (using the LED OB calibration runs), in the same way as the Laser OB, as a cross-check of the interline calibration has been recently started. The main difference is that the LED OBs have not enough power to illuminate with enough quality all the lines at the same time, making impossible a common frame to compare the offsets obtained by different OBs. A possible way to use this information is to consider

Line	Previous way	Auto-binning
1	-2.1	-2.1
2	-1.9	-2.1
3	0.8	0.5
4	----	----
5	-2.4	-2.2
6	-0.9	-0.9
7	-0.2	-0.3
8	7.1	7.5
9	1.0	0.8
10	-1.6	-1.3
11	----	----
12	----	----

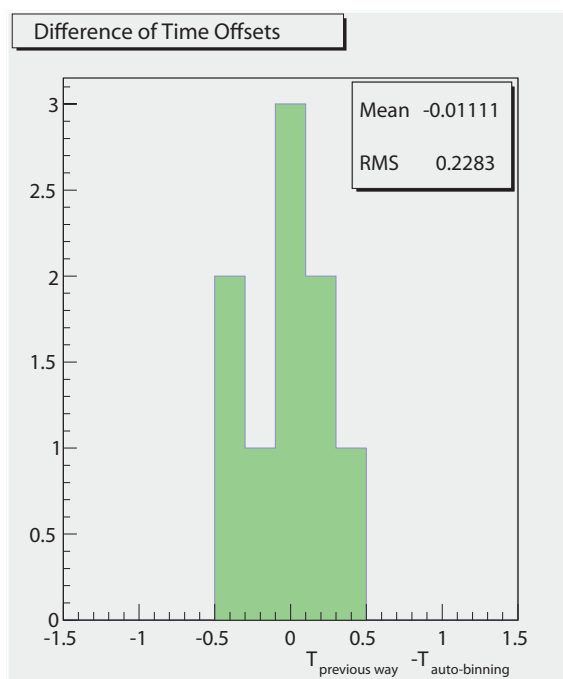


Figure 4.10: *left*: Table with the line offsets values obtained by the previous method and the ones computed with the auto-binning method; *right*: Distribution of the differences in the line offsets computed by both methods.

only the fit whose offset has been fitted with at least a minimum number of 6 floors in the fit and in a fit range larger than 30 m (see fig. 4.12 and Appendix C). The question is how to combine the different offsets obtained with each OB. For the time being, the most important result is that the offsets obtained with the LED OB are similar (differences of the order of one ns) to the ones obtained with the Laser OB.

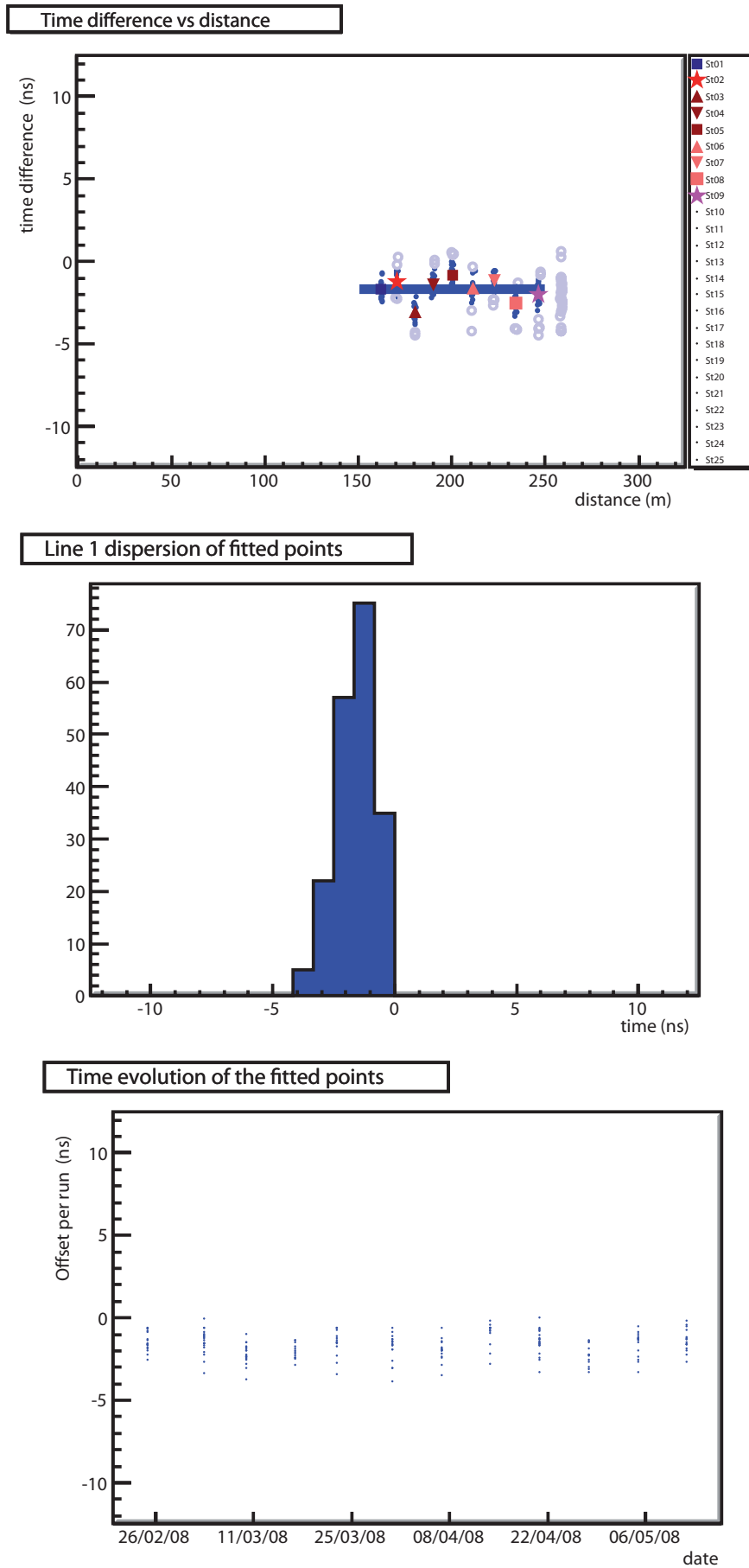


Figure 4.11: Example of the interline calibration of the line 1 with the Laser OB (12 runs).

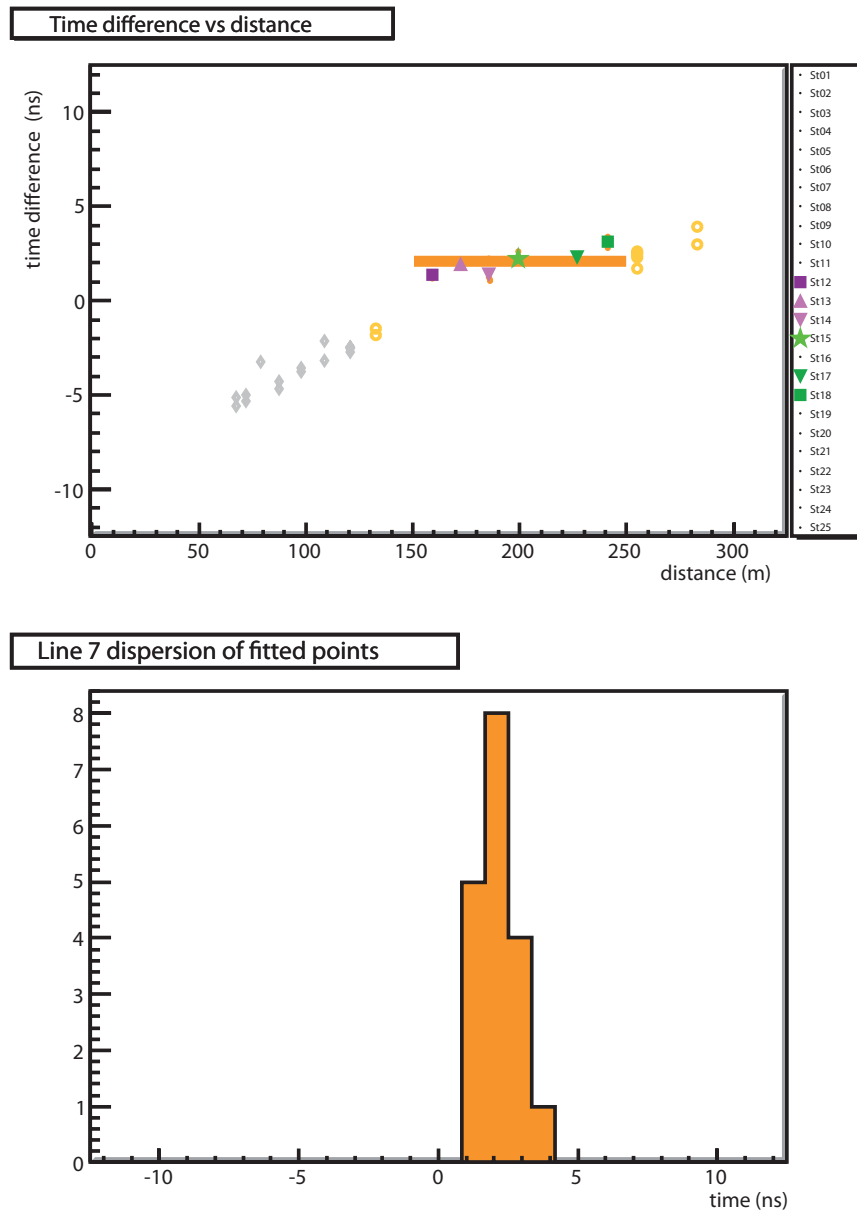


Figure 4.12: Example of the interline calibration of the line 7 with the LED OB of the line 9 floor 2 (only 1 run).



# Conclusions

In this Master's Thesis an automatic procedure for the time calibration of the detector ANTARES has been developed with the Optical Beacons system. The most important conclusions are the following:

- The time calibration is one of the most important aspects to take into account in a neutrino telescope.
- A new auto-binning algorithm which searches the best bin size to fit the hit arrival time distributions automatically has been developed (nearly 1800 histograms fitted), solving the needs of manual repair of the failed fits in the previous method.
- The new automated method is fast and reduces significantly the need of human intervention. The results are compatible with the previous method and the method is ready to be used.
- Ongoing studies about how to calibrate the first floors of the lines are promising.
- The evolution in time of the line offsets shows them as a stable parameter.
- LED OB can be used as a cross-check of the time offsets measured with the Laser OB.
- With the new automate procedure more calibration tables will be computed, including all the calibration periods, making the time calibration of the ANTARES neutrino telescope an easily updated and no very time consuming task.



# Appendix A

## Figures for the intraline calibration

Example fits of the intraline calibration of the line 1 (2 runs of LED OBs of line 1 plus one of the line 2 and another of the Laser OB, all of 18/02/2008).

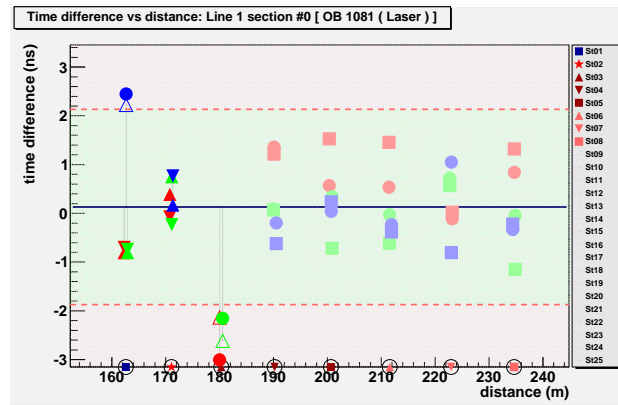


Figure A.1: Example of the intraline calibration of the *section #0* of the line 1 by the Laser OB.

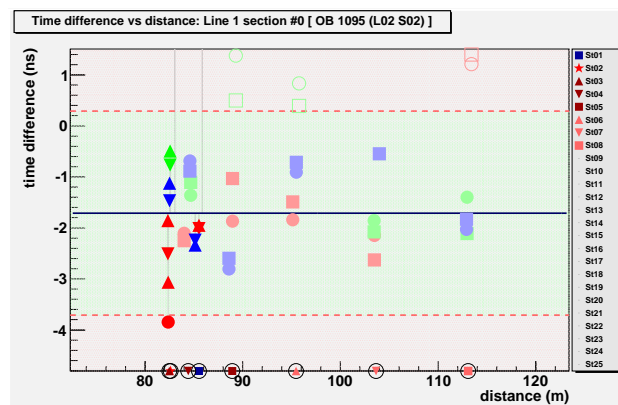


Figure A.2: Example of the intraline calibration of the *section #0* of the line 1 by the LED OB of the floor 2 in line 2.

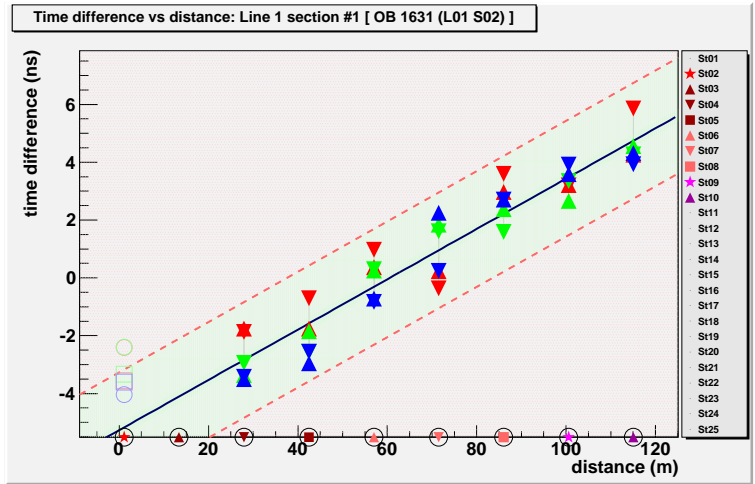


Figure A.3: Example of the intraline calibration of the *section #1* of the line 1.

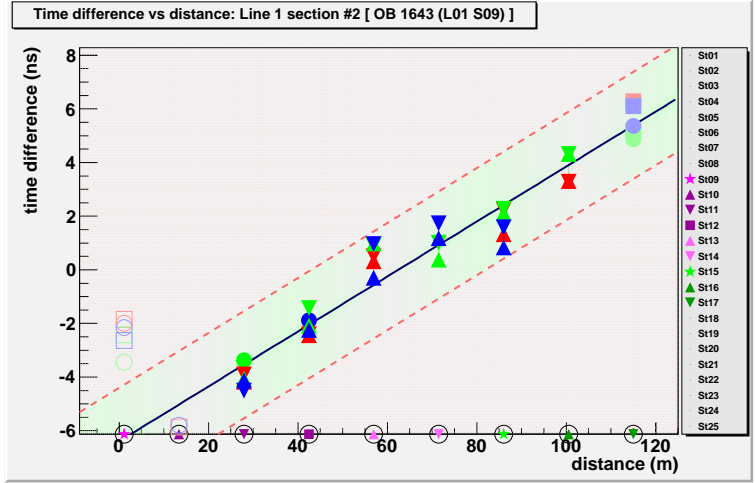


Figure A.4: Example of the intraline calibration of the *section #2* of the line 1.

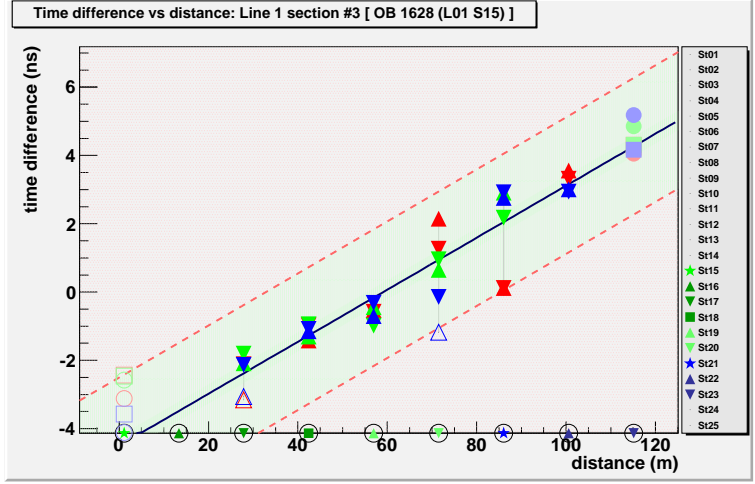


Figure A.5: Example of the intraline calibration of the *section #3* of the line 1.

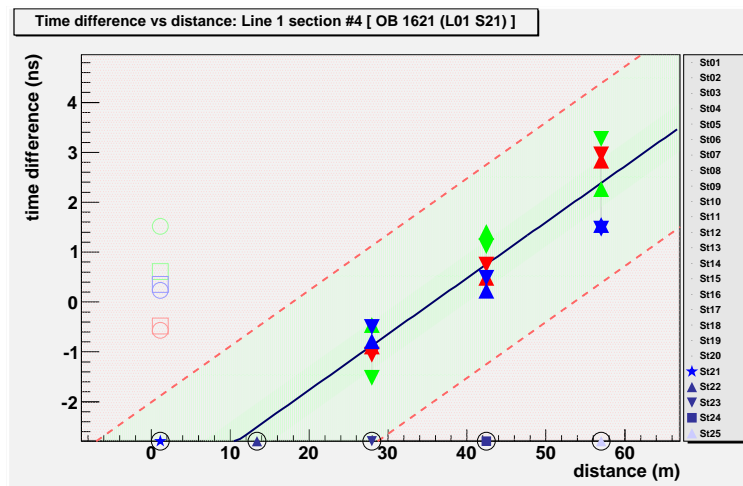


Figure A.6: Example of the intraline calibration of the *section #4* of the line 1.



# Appendix B

## Interline with the Laser OB

Example of the interline calibration of all the lines with the Laser OB (12 runs, from 25/02/2008 to 12/05/2008). Line 4 was not available for that period and lines 11 and 12 were not yet deployed.

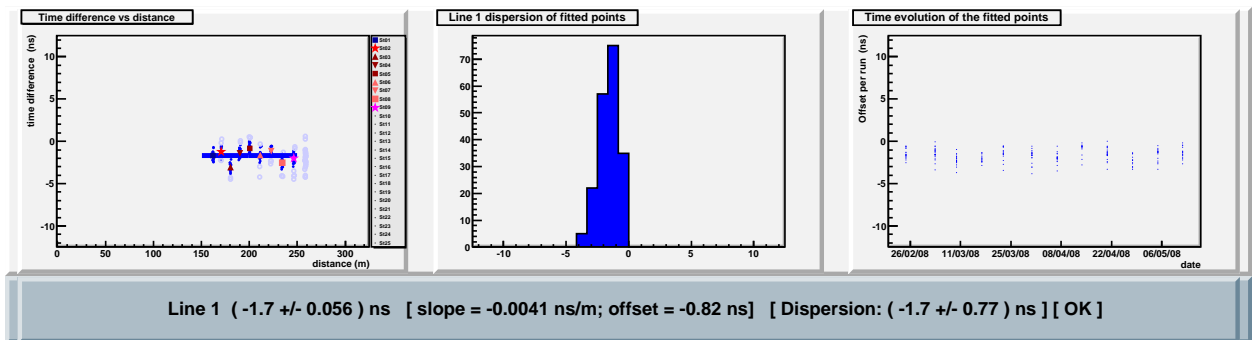


Figure B.1: Example of the interline calibration of the line 1 with the Laser OB (12 runs).

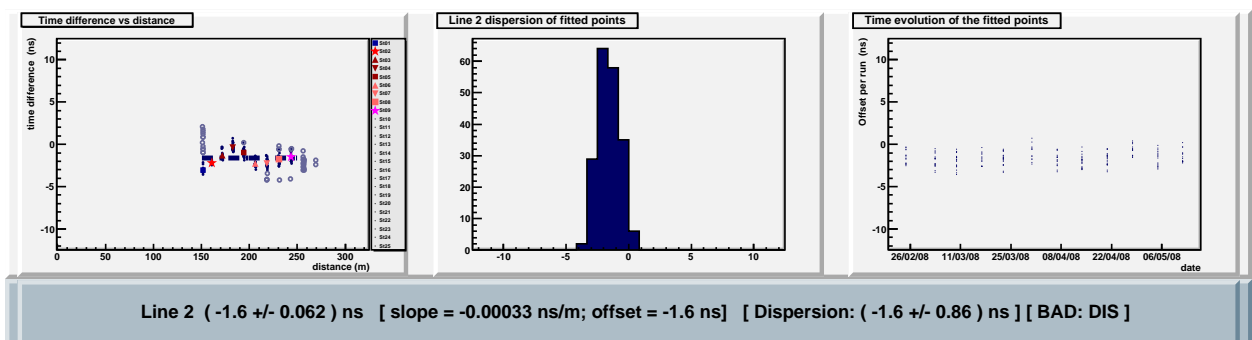


Figure B.2: Example of the interline calibration of the line 2 with the Laser OB (12 runs).

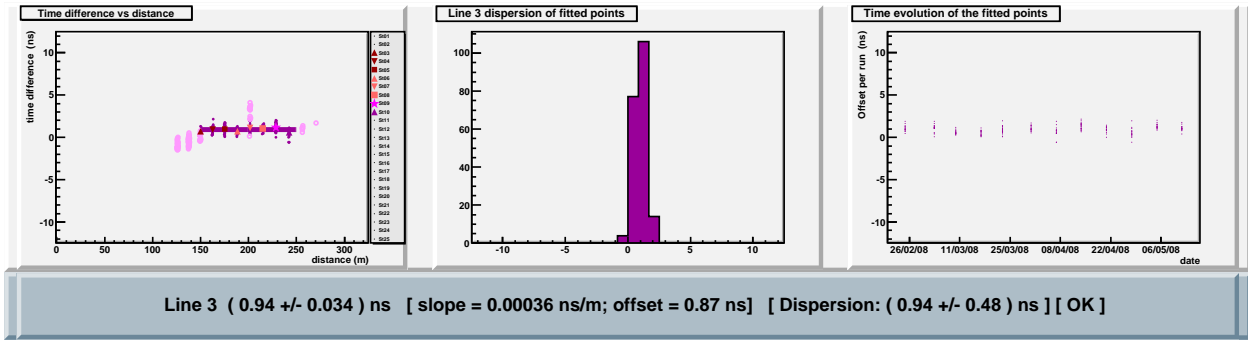


Figure B.3: Example of the interline calibration of the line 3 with the Laser OB (12 runs).

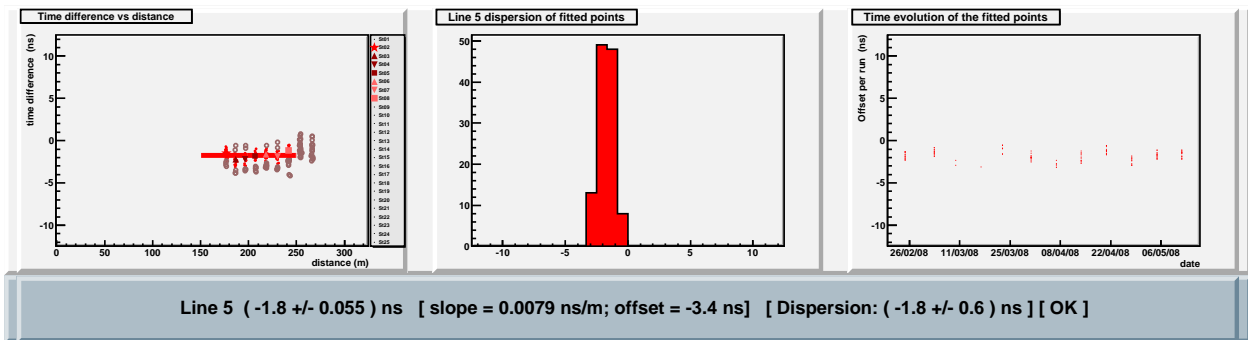


Figure B.4: Example of the interline calibration of the line 5 with the Laser OB (12 runs).

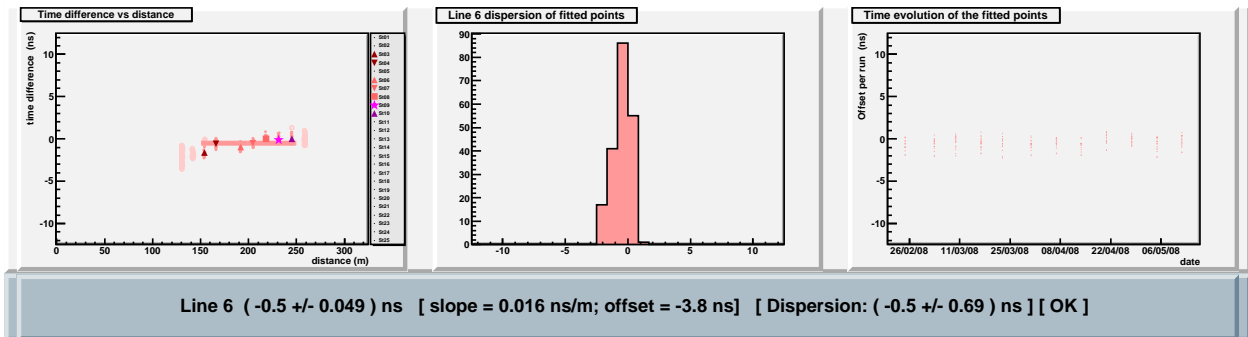


Figure B.5: Example of the interline calibration of the line 6 with the Laser OB (12 runs).

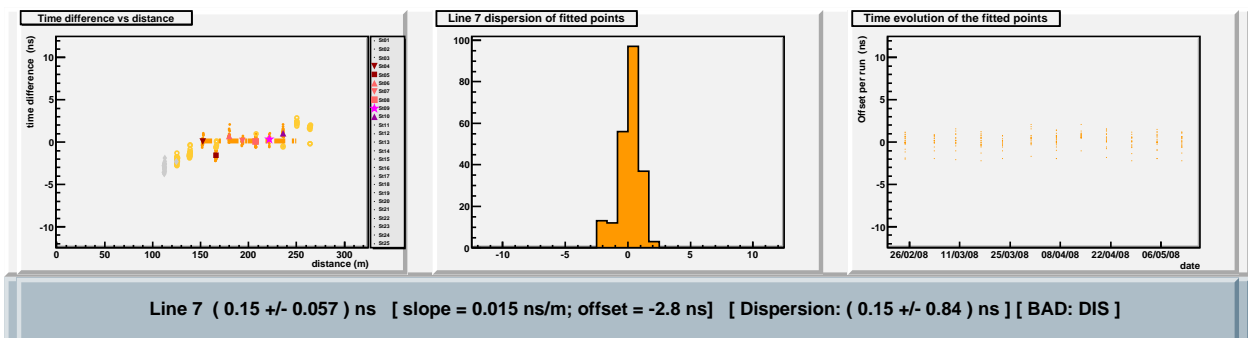


Figure B.6: Example of the interline calibration of the line 7 with the Laser OB (12 runs).

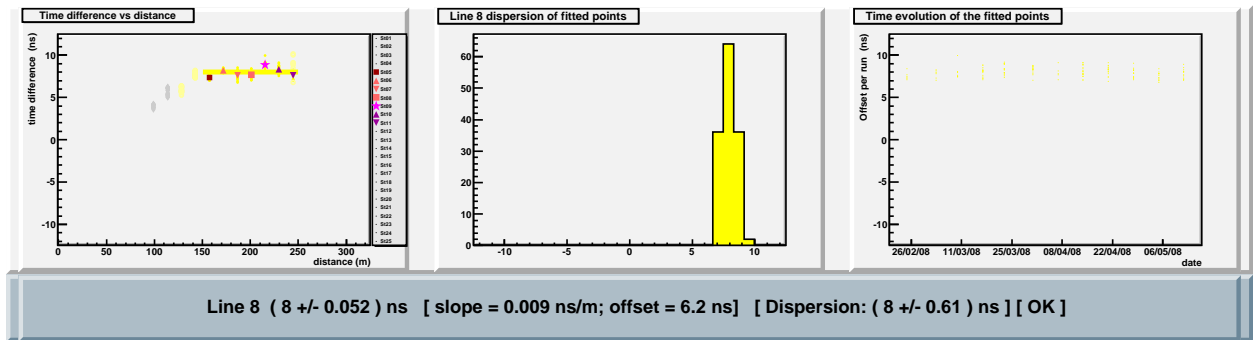


Figure B.7: Example of the interline calibration of the line 8 with the Laser OB (12 runs).

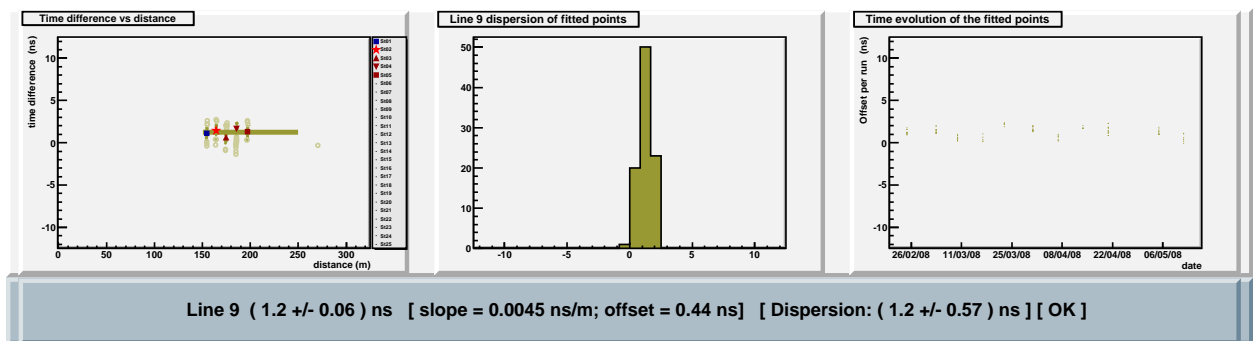


Figure B.8: Example of the interline calibration of the line 9 with the Laser OB (12 runs).

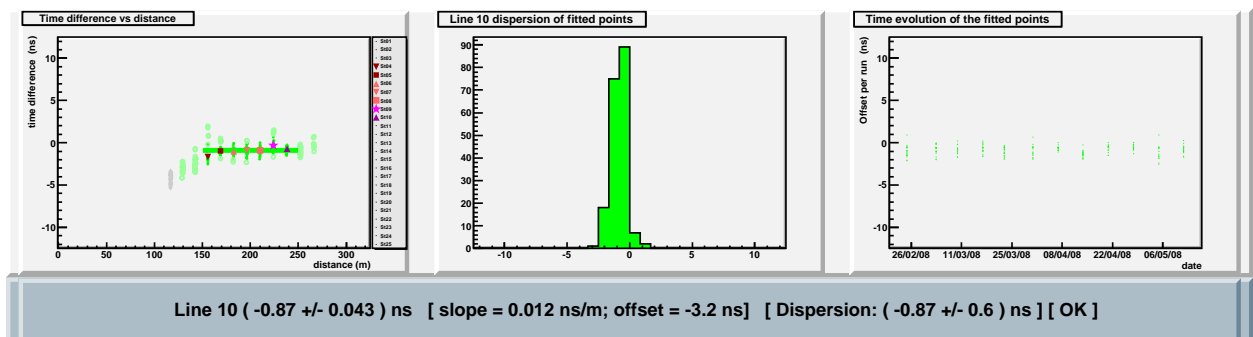


Figure B.9: Example of the interline calibration of the line 10 with the Laser OB (12 runs).

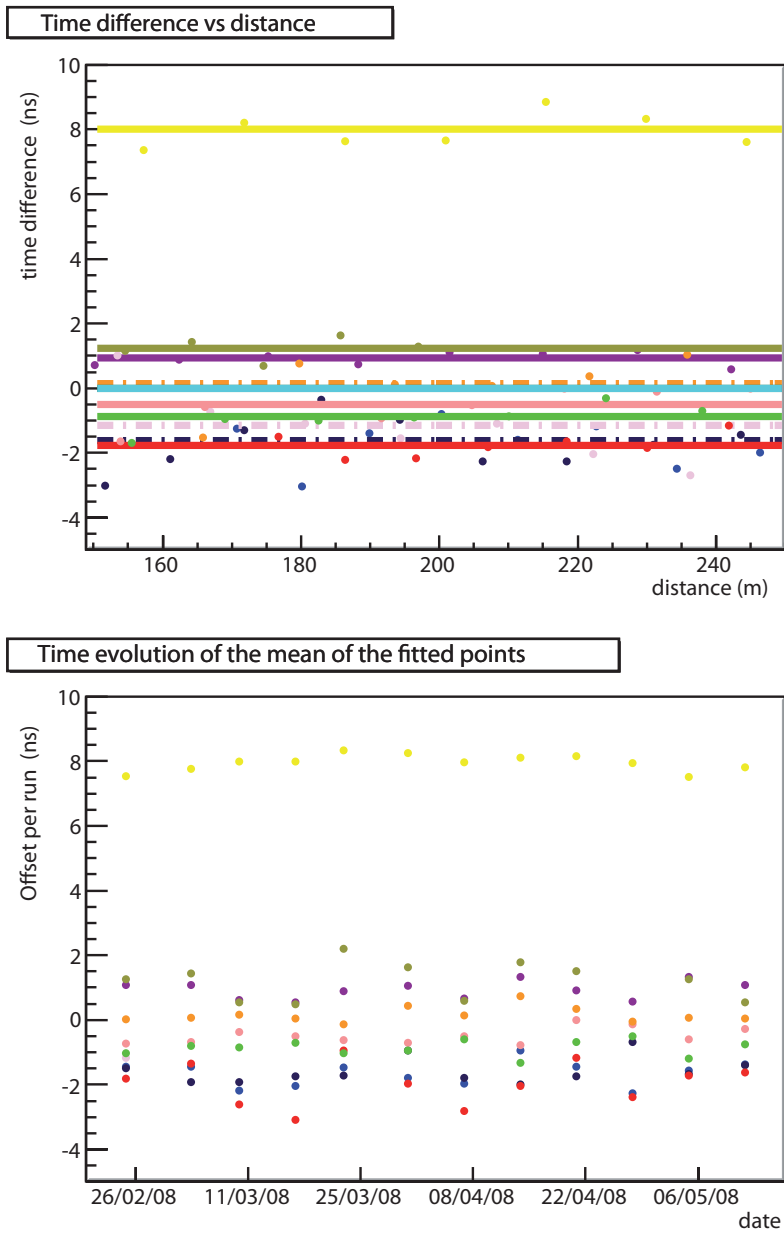


Figure B.10: Resume of the interline calibration with the Laser OB (12 runs).

# Appendix C

## Interline with the LED OB

Example of the interline calibration of some lines with different LED OBs (1 runs of 18/02/2008).

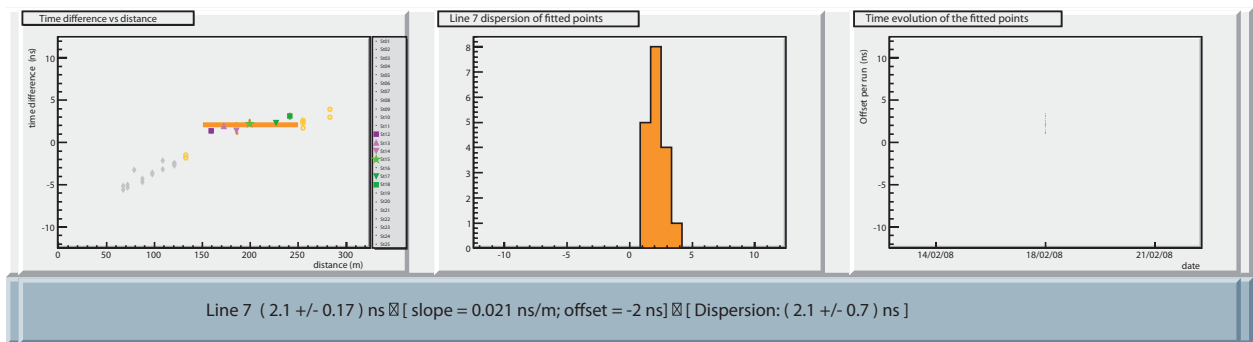


Figure C.1: Example of the interline calibration of the line 7 with the LED OB of the line 9 floor 2 (1 run).

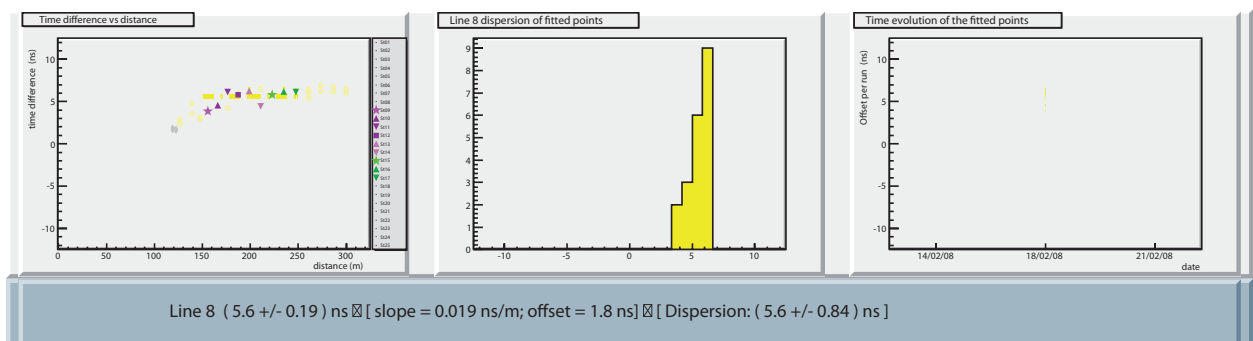


Figure C.2: Example of the interline calibration of the line 8 with the LED OB of the line 9 floor 2 (1 run).

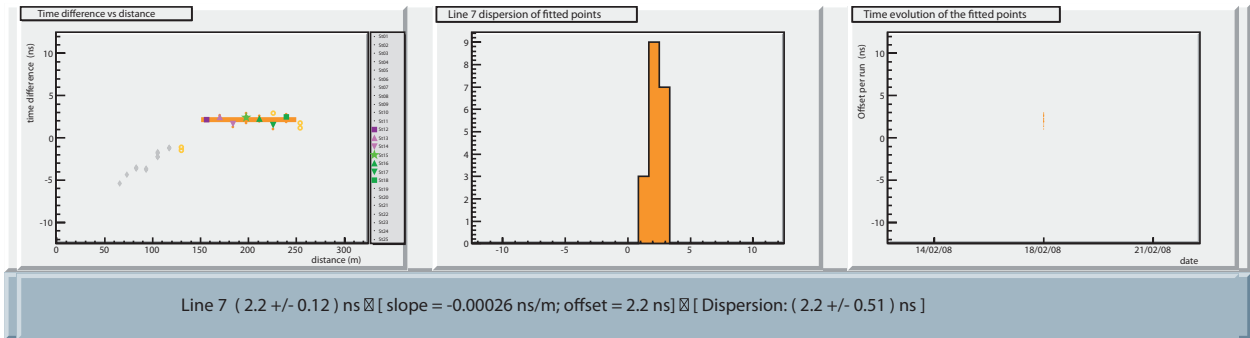


Figure C.3: Example of the interline calibration of the line 7 with the LED OB of the line 3 floor 2 (1 run).

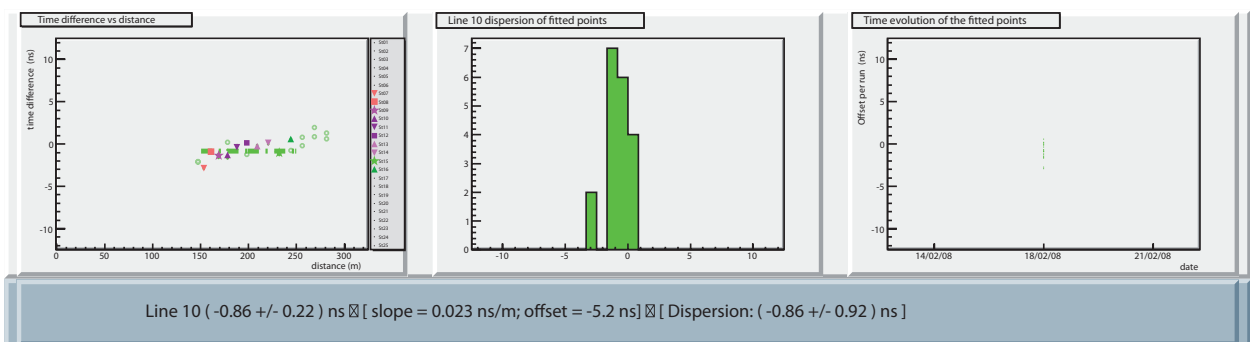


Figure C.4: Example of the interline calibration of the line 10 with the LED OB of the line 3 floor 2 (1 run).

# Bibliography

- [1] K. S. Hirata et al. Observation of  $^8\text{B}$  solar neutrinos in the Kamiokande-II detector. *Phys. Rev. Lett.*, 63:16, 1989.
- [2] K. S. Hirata et al. Observation of a neutrino burst from the supernova SN1987A. *Phys. Rev. Lett.*, 58:1490, 1987.
- [3] F. Halzen and E. Zas. Neutrino fluxes from active galaxies: A model-independent estimate. *Astrophys. J.*, 488:669, 1997.
- [4] J. Alvarez-Muniz and J. Meszaros. High energy neutrinos from radio-quiet active galactic nuclei. *Phys. Rev.*, D70:123001, 2004.
- [5] J. D. Hague. Correlation of the highest energy cosmic rays with nearby extragalactic objects in Pierre Auger Observatory data. 2009.
- [6] F. Halzen and A. O’Murchadha. Neutrinos from Auger sources. 2008. astro-ph/0802.0887v2.
- [7] E. Fermi. On the origin of cosmic rays. *Phys. Rev.*, 75(8):1169, 1949.
- [8] J. A. Hinton. The status of the H.E.S.S. project. *New Astron. Rev.*, 48:331–337, 2004.
- [9] F. Aharonian et al. Spectrum and variability of the Galactic Center VHE gamma-ray source HESS j1745-290. *Astron. & Astrophys.*, in press., 2009. astro-ph.GA/09061247.
- [10] F. Aharonian et al. Very high energy gamma rays from the direction of Sagittarius A\*. *Astron. & Astrophys. Astron. Astrophys. 425 (2004) L13-L17*, 2004.
- [11] J. Albert et al. (MAGIC Collaboration). Variable very high energy gamma-ray emission from the microquasar LS I+61 303. *Science*, 312:1771, 2006. astro-ph/0605549.
- [12] D. F. Torres and F. Halzen. LS I+61 303 as a potential neutrino source on the light of MAGIC results. 2006. astro-ph/0607368.
- [13] W. Bednarek. Propagation of very high energy gamma-rays inside massive binaries LS 5039 and LSI +61 303. 2006. astro-ph/0601657.
- [14] J. Rico et al. Status and recent results on magic. *Contribution to the Proceedings of Science with the new generation of high energy gamma-ray experiments, Abano Terme, Italy, 8-10 October 2008*.
- [15] The ANTARES Collaboration. A Deep Sea Telescope for High Energy Neutrinos. Proposal for a 0.1 km<sup>2</sup> detector, 1999.

- [16] P. Amram et al. The ANTARES Optical Module. *Nucl. Instr. and Methods A484 (2002) 369*, 2002.
- [17] M. Ageron et al. (The ANTARES Collaboration). The ANTARES Optical Beacon System. *Nucl.Instrum.Meth.A578:498-509,2007*, 2007.
- [18] The ANTARES Collaboration. Performance of the front-end electronics of the ANTARES neutrino telescope. 2010. arXiv:1007.2549.
- [19] F. Salesa-Greus. ANTARES time calibration. *Nucl. Inst. and Meth. in Phys. Res. A602 (2009) 7275*, 2009.
- [20] J.P. Gómez-González. Timing Calibration in ANTARES. *Proceedings of the 31th ICRC*, 2009.
- [21] F. Salesa. Time Calibration and Point Source Analysis with the ANTARES Neutrino Telescope. PhD thesis, University of Valencia, Spain, 2010.